1999

Resonance production in quark and gluon jets

Derek William Lane
Iowa State University

INFORMATION TO USERS

This manuscript has been reproduced from the microfilm master. UMI films the text directly from the original or copy submitted. Thus, some thesis and dissertation copies are in typewriter face, while others may be from any type of computer printer.

The quality of this reproduction is dependent upon the quality of the copy submitted. Broken or indistinct print, colored or poor quality illustrations and photographs, print bleedthrough, substandard margins, and improper alignment can adversely affect reproduction.

In the unlikely event that the author did not send UMI a complete manuscript and there are missing pages, these will be noted. Also, if unauthorized copyright material had to be removed, a note will indicate the deletion.

Oversize materials (e.g., maps, drawings, charts) are reproduced by sectioning the original, beginning at the upper left-hand corner and continuing from left to right in equal sections with small overlaps. Each original is also photographed in one exposure and is included in reduced form at the back of the book.

Photographs included in the original manuscript have been reproduced xerographically in this copy. Higher quality 6" x 9" black and white photographic prints are available for any photographs or illustrations appearing in this copy for an additional charge. Contact UMI directly to order.

UMI

A Bell & Howell Information Company
300 North Zeeb Road, Ann Arbor MI 48106-1346 USA
313/761-4700 800/521-0600

Resonance production in quark and gluon jets

by

Derek William Lane

A dissertation submitted to the graduate faculty

in partial fulfillment of the requirements for the degree of

DOCTOR OF PHILOSOPHY

Major: High Energy Physics

Major Professor: Eli Rosenberg

Iowa State University

Ames, Iowa

1999

Graduate College
Iowa State University

This is to certify that the Doctoral dissertation of

Derek William Lane

has met the dissertation requirements of Iowa State University

Signature was redacted for privacy.

Major Professor

Signature was redacted for privacy.

For the Major Program

Signature was redacted for privacy.

For the Graduate College

TABLE OF CONTENTS

LIST OF TABLES

LIST OF FIGURES

ABSTRACT

The formation of hadrons from free quarks and gluons is poorly understood and can not be fully explained by current theories. This hadronization process is described using phenomenological models, each reflecting possible scenarios for the QCD dynamics. Electron-positron annihilation at the Z^0 resonance provides an ideal environment in which to study hadron production because of the combination of high event rates and clean final states due to the absence of beam and target remnants. Using the particle identification capabilities of the DELPHI detector at the Large Electron-Positron collider (LEP), it is possible to differentiate the production of different hadron species in the final state. This information allows the study of details of the transition from quarks and qluons to stable hadrons. This thesis investigates the hadronization process by comparing the production of ϕ and K^{*0} particles produced in quark jets versus those produced in gluon jets at the Z^0.

CHAPTER 1 INTRODUCTION

Throughout the centuries, mankind has sought to understand and explain the world around him. Around 400BC, the greek philosopher Democritus theorized that every kind of matter could be subdivided into smaller and smaller pieces until one arrived at a basic building block which could no longer be divided into smaller pieces. He named these "atoms", which means uncuttable. His ideas were ignored for almost two millenia until the early 1800s when they were picked up and refined slightly to become the basis of our modern atomic theory, i.e. that all known elements are formed of indivisible atoms from which the elements derive their properties [1]. Around the beginning of the twentieth century, it was shown that atoms, despite their name, *were* divisible, being made up of electrons and nuclei. Later, it was found that nuclei could be further subdivided into two types of nucleons: protons and neutrons. As more investigations were made of the subatomic realm, more particles were discovered with masses between that of the electron and those of the nucleons and were given the name "mesons" from the greek word *mesos* meaning "middle." And the complexity didn't stop there. A heavier version of the electron was discovered in cosmic rays and given the name "muon." Other particles which were heavy like the nucleons appeared and were called "baryons" from the greek word *barus* meaning "heavy." Collectively mesons and baryons are called *hadrons* because they interact via the strong force. Likewise, the electrons and electron-like particles, along with other particles called neutrinos, are called *leptons*. In the early 1960s, a theory was proposed to explain the hadrons as being composed of even smaller particles called quarks. This description of matter, in terms of quarks and electron-like

particles, has been able to explain quite well most observations of the subatomic world and has come to be known as the Standard Model of Particles and Fields.

This "Standard Model" holds that matter is made up of a few basic building blocks (see Figure 1.1). The particles are arranged into three generations. The first generation (marked with an I in Figure 1.1) contains an up quark, a down quark, an electron, and a particle associated with the electron called an electron neutrino (ν_e). Most ordinary, stable matter is composed of these particles. The other two generations are similar but tend to be more massive. In addition to the particles, there are four known forces: electromagnetism, the strong nuclear force, the weak force, and gravity. Electromagnetism is carried by the photon (γ), the strong nuclear force, which is now called the color force, is carried by the gluon (g) (so called because it is the "glue" that binds quarks together to make composite particles), the weak force is carried by the W and Z particles, and gravity is carried by the theoretically surmised graviton.

Quarks can be combined into composite particles (the mesons and baryons mentioned earlier). For example, two up-quarks and one down-quark (uud) form a proton whereas one up-quark and two down-quarks (udd) form a neutron. Three-quark combinations are baryons and there are many of them depending which types of quarks (up, down, charm, strange, top, bottom) are put together. Antibaryons, which are anti-matter baryons, are formed by combining three anti-matter quarks (a.k.a. antiquarks). Combining a quark with an antiquark gives a meson. Some baryon and meson combinations are shown schematically in Figures 1.2 and 1.3, respectively.

Particle physics today is carried out using powerful accelerators. These machines take a beam of particles such as electrons or protons, accelerate them to high energies, and then smash them into a fixed target or head-on into another high energy beam of particles. The reason for using high energies is twofold; first, the wavelength of the particles gets shorter as the energy increases, thus it becomes possible to study matter at smaller scales, and secondly, higher energies are needed to produce the more exotic

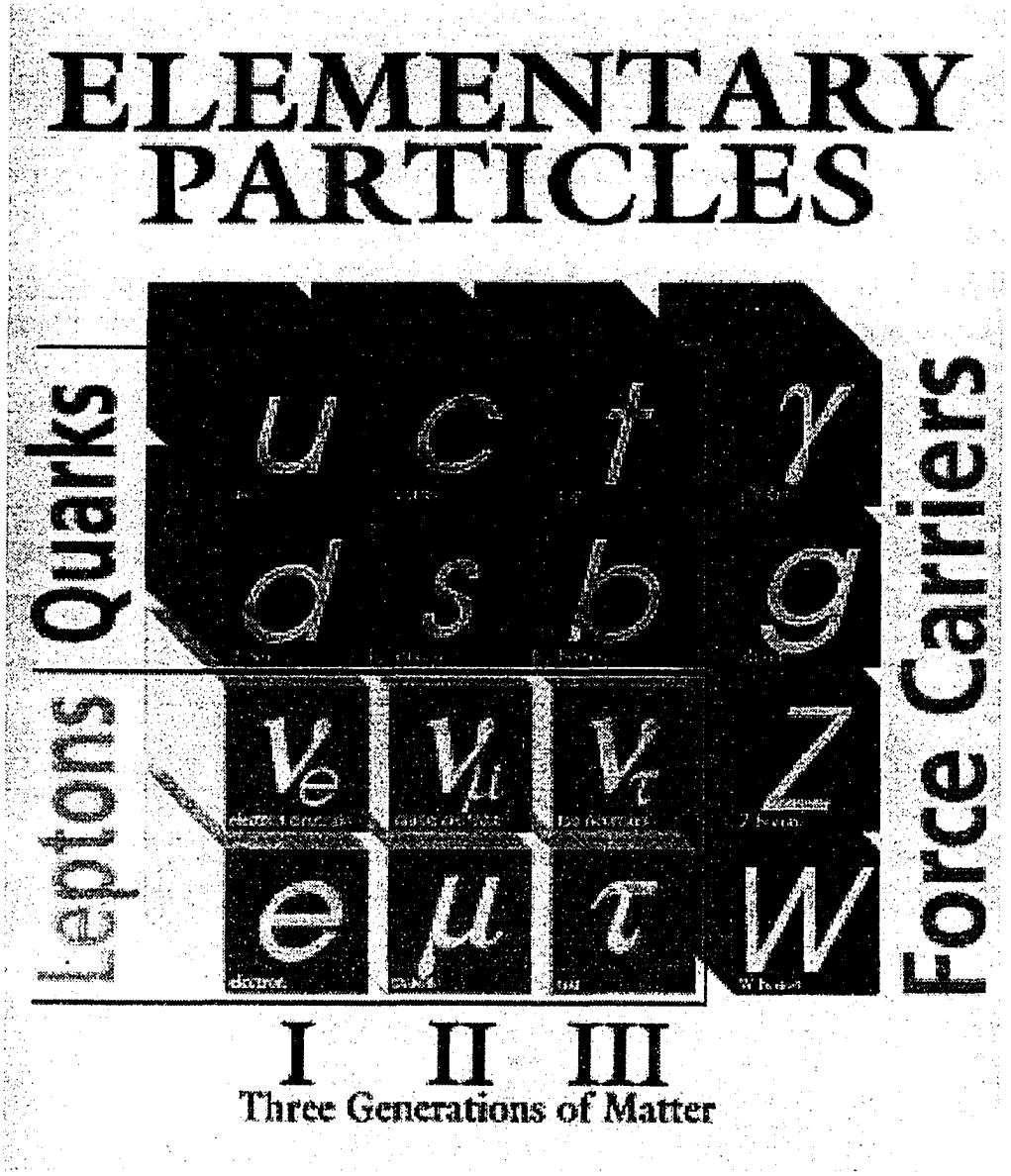

Figure 1.1 The fundamental particles known to date. Most ordinary matter is made up of the particles in Generation I [2].

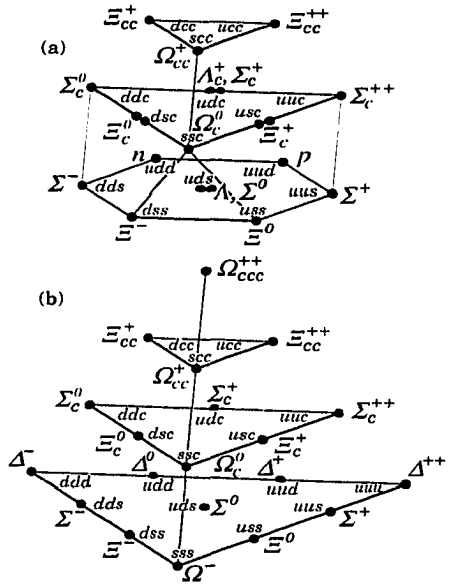

Figure 1.2 Some of the baryons formed by combining the four lightest quarks u, d, s, and c [3].

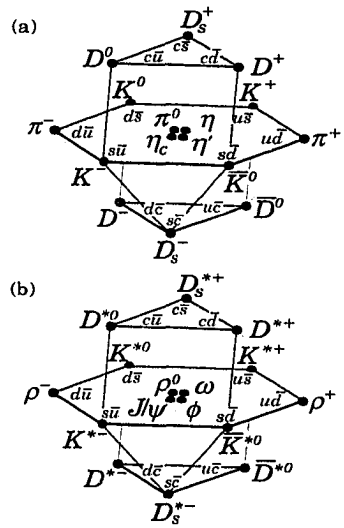

Figure 1.3 Some of the mesons formed by combining the four lightest quarks u, d, s, and c [3].

particles in the subatomic realm, some of which have high masses [4].

One example of an accelerator is the Large Electron-Positron accelerator at the European Laboratory for Particle Physics (CERN) located near Geneva, Switzerland. There beams of electrons and anti-electrons (also called positrons) are collided at high energy in order to produce other particles. One possibility is that they produce two quarks, which then spawn other quarks, etc. , and finally all these quarks combine to form mesons and baryons (see Figure 1.4). The Standard Model and quantum mechanics can describe the formation of quarks from the electron-positron collision and they also do a good job of describing the properties of the mesons and baryons formed from quarks. However, the theory still can not describe the transition phase in which the free quarks actually get together and form mesons and baryons. Physicists must construct models to try to describe what is happening and many schemes have been proposed. Selecting between them can only be done by doing more experiments and discovering the details of the hadron formation process.

My analysis, which I present in this thesis, attempts to fill in one small piece of the puzzle by making a measurement of specific hadrons produced in collisions at LEP. With enough such pieces, physicists may one day be able to accurately describe the hadronization process.

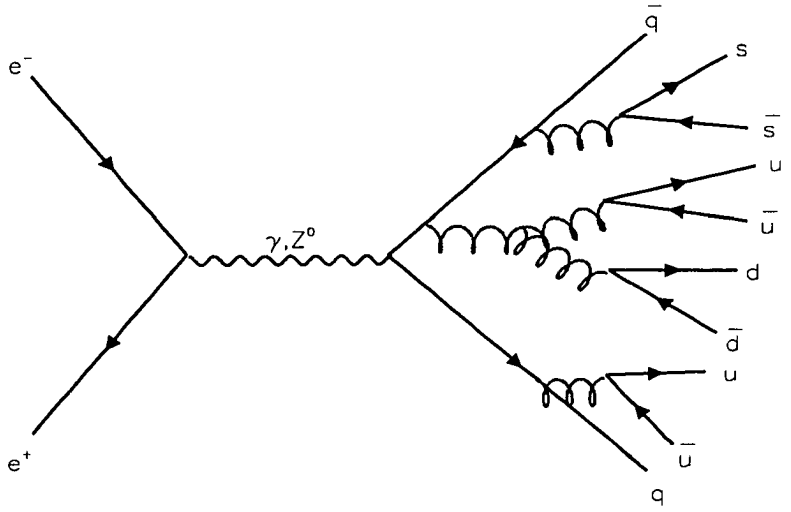

Figure 1.4 Schematic representing the collision of an electron and positron. An intermediate photon (γ) or Z^0 particle is created which then decays to two quarks. The quarks then radiate gluons, which split into more quarks, and so on. Eventually, all the quarks produced will bind together to form hadrons.

CHAPTER 2 THEORY

Hadrons produced in e+e- reactions have their origin in a simple quark-anti-quark configuration. The theory known as the Standard Model of Particle Physics gives an excellent description of how these quarks are produced from the electron-positron collision. These two quarks initiate the production of numerous mesons and baryons which are actually observed in the laboratory. This is usually broken down into two processes: one in which the two primary quarks produce a shower of secondary quarks and gluons followed by another by which these secondary quarks and gluons are combined into the final state mesons and baryons. Quarks and gluons are also called partons, hence the first process is referred to as the parton shower. It can be described by perturbative Quantum Chromodynamics (pQCD) which reproduces fairly well the global properties of hadronic events. From here, the non-perturbative hadronization process is invoked to describe how hadrons are produced from the partons in the shower. It is at this point that models differ the most, each giving a good overall description of the event but differing in the details. The only way to choose between models and achieve a clearer understanding of the hadronization process is to examine the details of real hadronic events.

This chapter begins with an overview of electroweak physics and the production of the initial quark and antiquark, followed by a brief description of the parton shower. We then discuss the hadronization process and give an overview of the currently popular models used to describe it.

2.1 Producing the Initial Quarks

At LEP, electrons and positrons annihilate to either a virtual photon or a Z^0 boson, which subsequently decays to a fermion-anti-fermion pair (Figure 2.1). This $f\overline{f}$ pair can be any of the elementary fermions, i.e. leptons (e^+e^-, $\mu^+\mu^-$, $\tau^+\tau^-$, $\nu_e\overline{\nu_e}$, $\nu_\mu\overline{\nu_\mu}$, $\nu_\tau\overline{\nu_\tau}$) or quarks ($d\overline{d}$,$u\overline{u}$,$s\overline{s}$,$c\overline{c}$, $b\overline{b}$, but not $t\overline{t}$ which is too massive to be produced at LEP, which has only half as much energy as would be necessary to produce a $t\overline{t}$ pair). When two quarks are produced, the picture is more complicated because they can radiate gluons in a showering process which results in many final state hadrons (Figure 2.2).

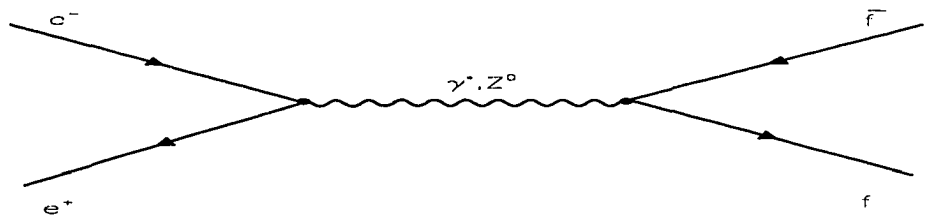

Figure 2.1 The reaction $e^+e^- \rightarrow \gamma^*, Z^0 \rightarrow f\overline{f}$.

Taking into account that each quark comes in three colors, this means that there are 6 lepton decay modes and 15 quark decay modes, for a total of 21. Assuming massless fermions, which is a reasonable approximation to make since the collision energy of 91 GeV is far above the masses of the fermions produced (0-5 GeV), the relative branching fractions can be calculated simply by counting states, i.e. $\mathrm{BF}_{leptons} = \frac{6}{21} \approx 29\%$ and $\mathrm{BF}_{quarks} = \frac{15}{21} \approx 72\%$, although the actual values are shifted due to mass and phase space effects and the fact that the couplings are different, too.. This explains why the hadronic

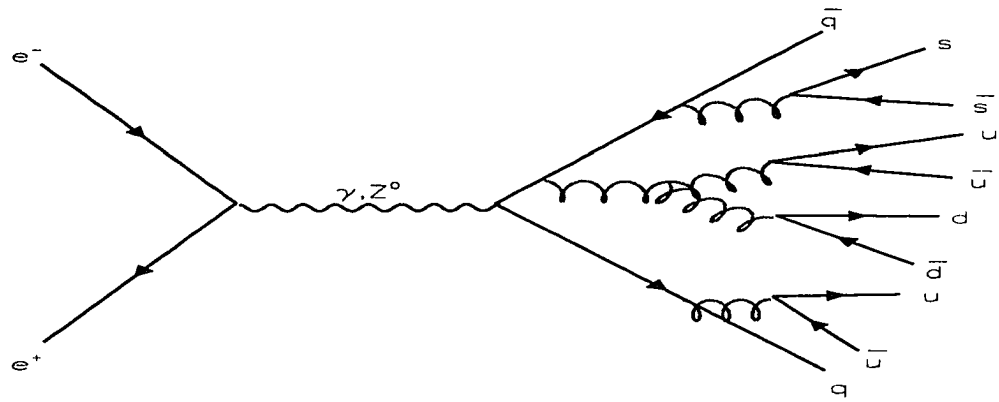

Figure 2.2 The hadronization process. The quarks initiate a shower of secondary partons, all of which combine to form hadrons.

cross section at LEP I is so much higher than the leptonic cross section. Figure 2.3 shows the relative branching fractions for quarks as a function of the center of mass energy of the collision. LEP runs at the Z^0 mass which is 91GeV.

The charged lepton decay modes are clean events, characterized by two colinear tracks each with an energy of half of the total energy, i.e. $\frac{\sqrt{s}}{2}$. Figures 2.4 and 2.5 show actual electron and muon events recorded by DELPHI, one of the four detectors located on LEP. Tau events are different because the τ decays without travelling very far, thus $\tau^+\tau^-$ events appear a two jets with low multiplicity and often missing energy (i.e. energy carried away by neutrinos). See Figures 2.6 and 2.7.

2.2 Parton Shower

Quark events are more complex because the color field between the quarks spawns more quarks, which join with each other and with the original quarks to form hadrons.

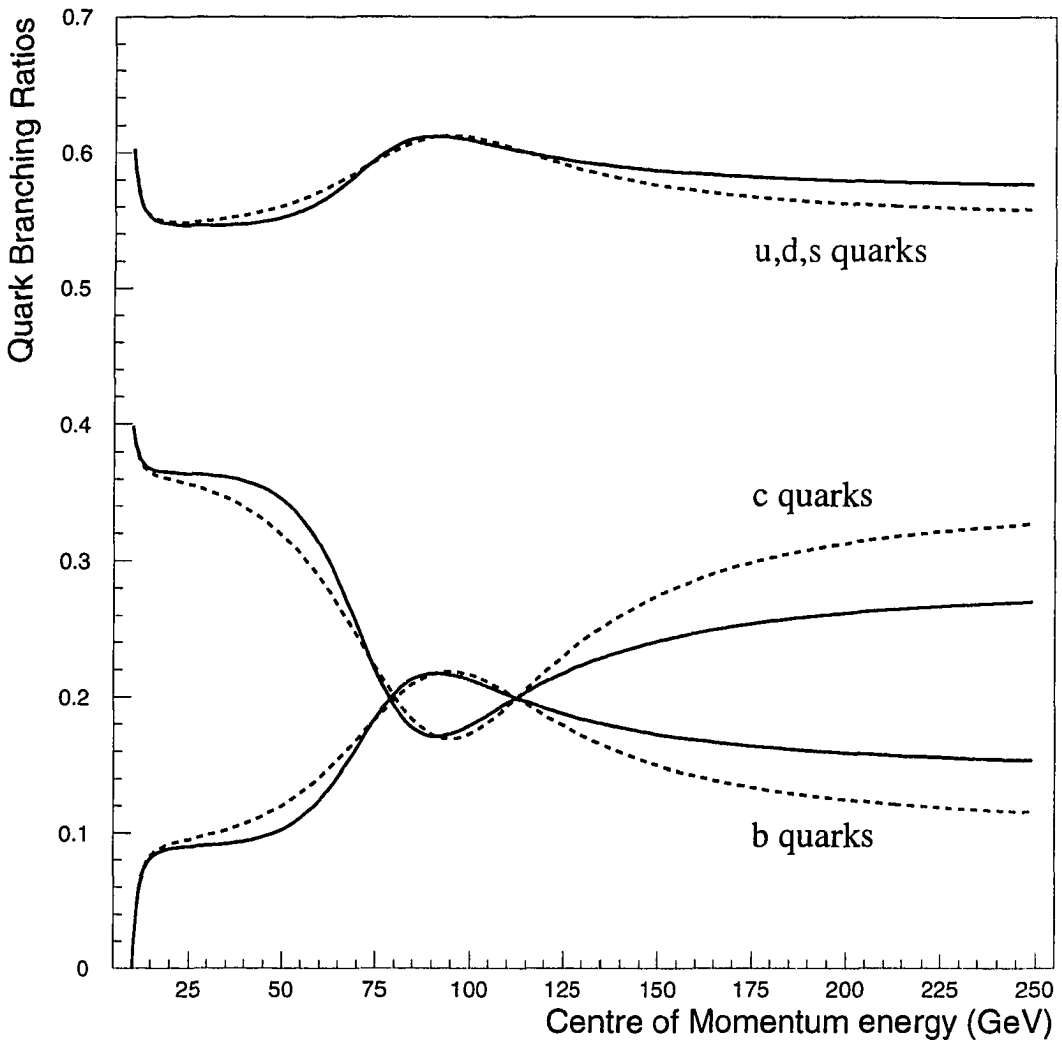

Figure 2.3 Branching fractions for $e^+e^- \rightarrow \gamma^*, Z^0 \rightarrow f\overline{f}$ as a function of the center of mass energy $\sqrt{s}$. (Figure taken from Knowles and Lafferty [6].)

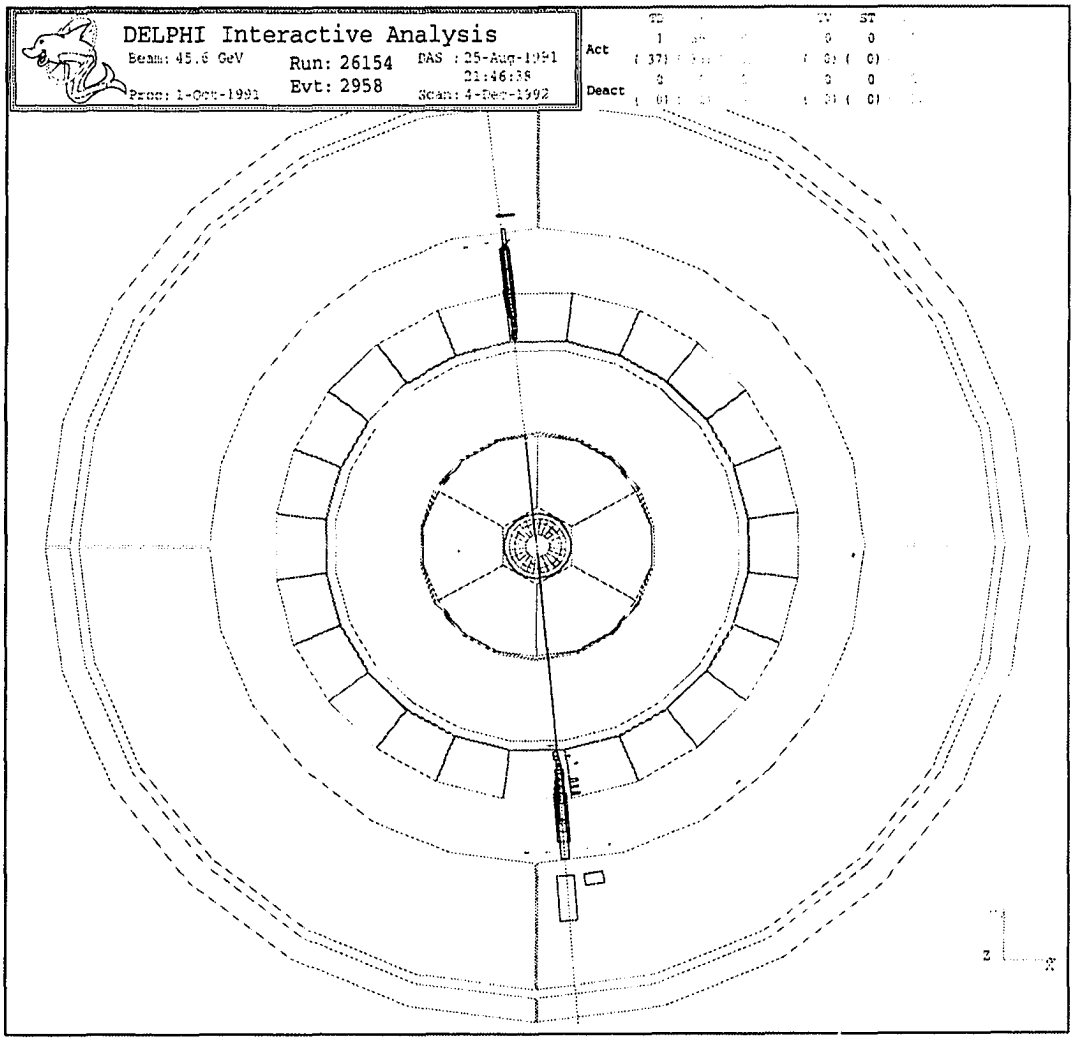

Figure 2.4 An $e^+e^- \to e^+e^-$ event showing the charged electron tracks and energy deposition in the electromagnetic calorimeter. (Note the energy deposition in the calorimeter to the right of the lower track and the fact that the two tracks are not quite colinear. This indicates that the lower electron radiated a photon. Such radiated photons, also called δ-rays, are common for electrons in DELPHI due to the accelerating effect of the magnetic field on the relatively light electrons.)

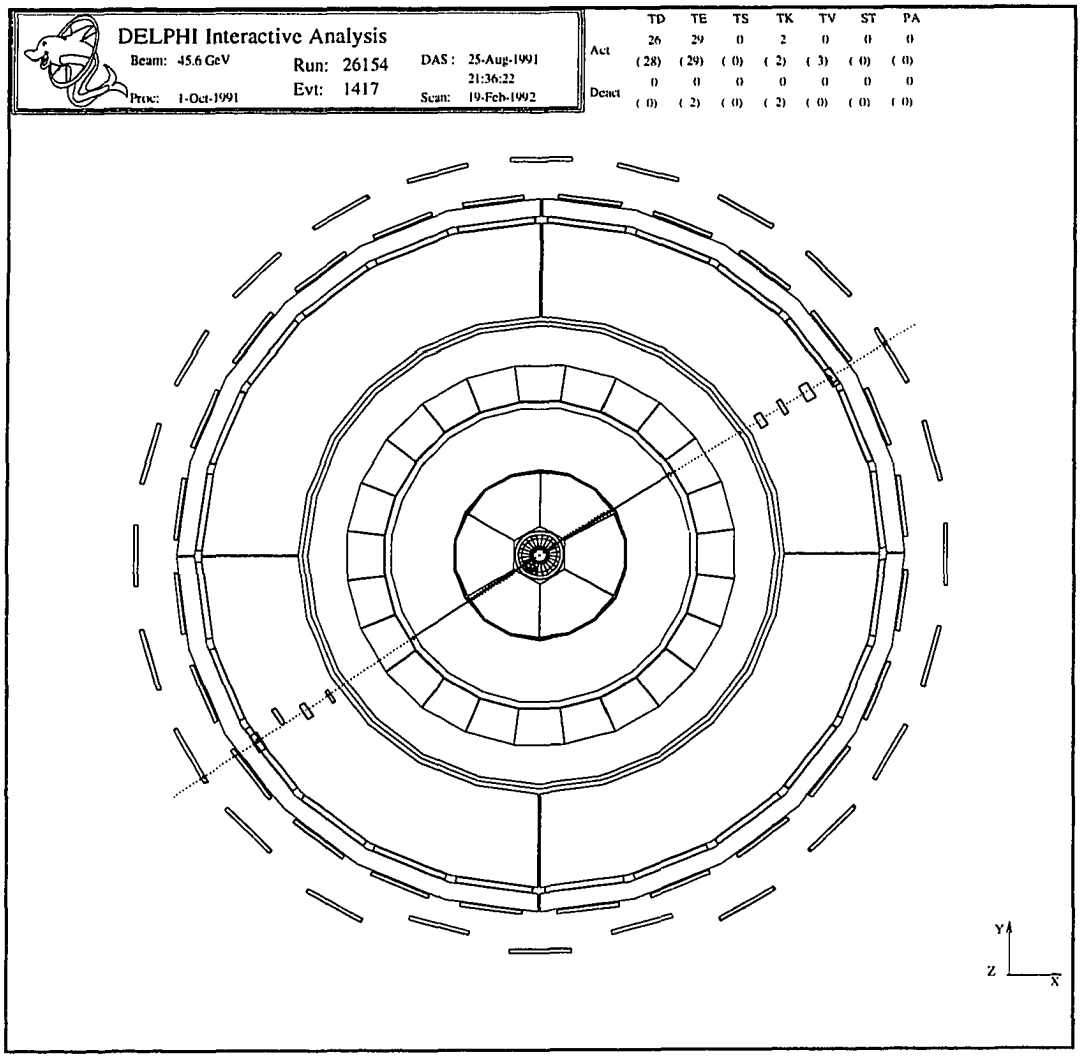

Figure 2.5 An $e^+e^- \rightarrow \mu^+\mu^-$ event showing the charged muon tracks and the telltale hits in the muon detector. (Note that the view on this plot has been widened in order to include the muon chambers.)

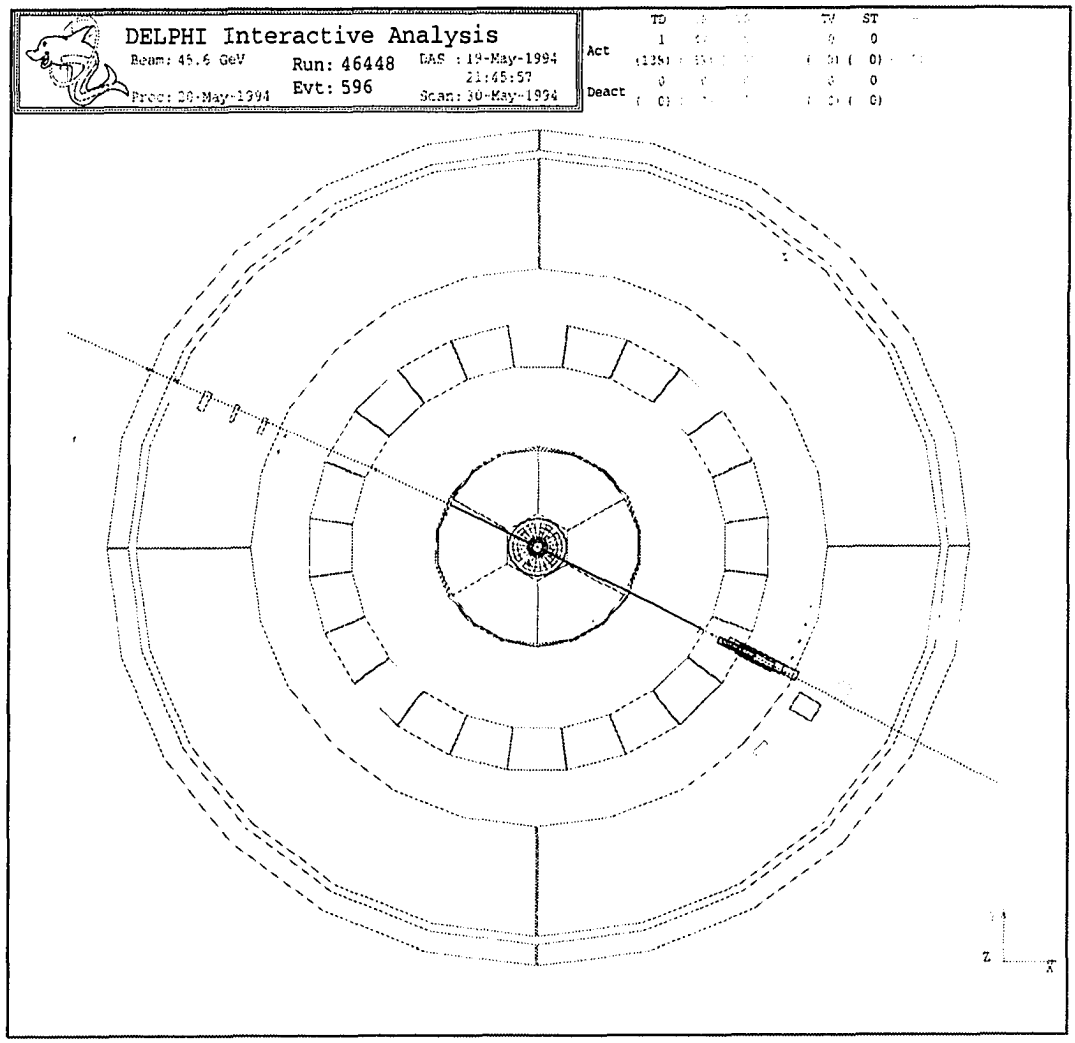

Figure 2.6 An $e^+e^- \to \tau^+\tau^-$ event. Although visually this looks like the e^+e^- and $\mu^+\mu^-$ events, one can tell that the τs have decayed, one to an electron and the other to a muon, because of the energy depositon in the electromagnetic calorimeter and the hits in the muon chambers, respectively.

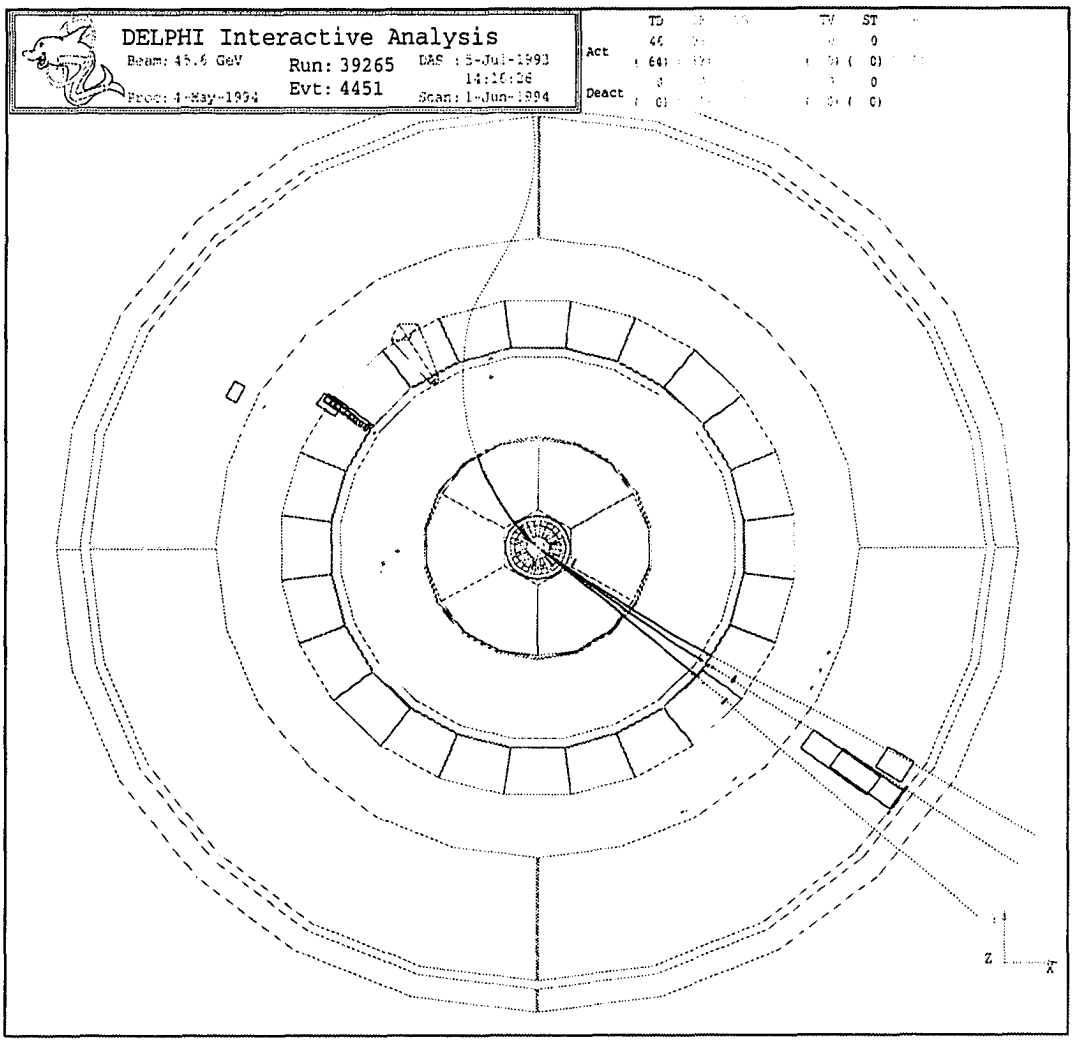

Figure 2.7 An $e^+e^- \rightarrow \tau^+\tau^- \rightarrow (2hadronjets)$ event, where one τ-jet has three charged particles in it.

What one sees is two jets of hadrons, as depicted in Figure 2.8. This is further complicated when one of the quarks radiates a hard gluon which forms another jet of hadrons. This can happen multiple times, causing many-jet hadronic events.

There are typically around 30 hadrons produced in an hadronic event at LEP I. The way in which quarks and gluons eventually form hadrons is as yet undetermined. Current models [8, 9, 10, 11] represent the color field between the quarks as a narrow flux-tube typically of width ~1fm. The energy density in the tube increases linearly with the separation between the quarks (except for a short-range Coulomb term). As the quarks separate, the energy between them becomes great enough to form $q\bar{q}$ pairs. Most models use some combination of pQCD, which describes the shower of quarks and gluons down to some energy scale Q_0, and a phenomenological picture of how the resulting partons actually combine to form hadrons (Figure 2.9). This follows because, in the early stages while particle energies are still high, the strong coupling constant α_s is small and one can make a perturbative expansion of the terms in the QCD Lagrangian and thus calculate the dominant terms in the shower evolution. Quarks can emit gluons, gluons can form $q\bar{q}$ pairs or branch to more gluons, all in a repeating process until the quarks and gluons have too little energy to continue the showering process. At this point, they combine into stable hadrons, either as $q\bar{q}$ meson states (such as π, ω, K, η,

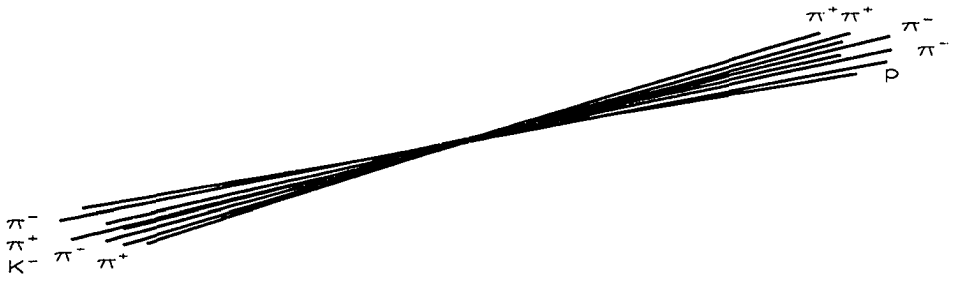

Figure 2.8 2-jet hadronic event.

ϕ, etc.) or qqq baryon states (such as p, n, Λ, Σ, etc.). Many of the global features of an event, such as multiplicity, event shapes, energy dependences, etc., can be described by the parton shower in pQCD [12]. The shower cutoff Q_0 is typically on the order of 1 GeV, though some recent papers [13, 14, 15, 16, 17] argue that it can be taken much lower, even down to the level of typical hadron masses, i.e. around a few hundred MeV. It is not possible for pQCD to describe the shower at low energies because the strong coupling constant becomes large, making the perturbative expansion no longer valid.

2.3 Hadronization

While pQCD gives a good description of the global properties of hadronic events, the actual mechanism in which the partons in the shower form observable hadrons remains undetermined and subject to a certain amount of speculation. At this point, one must turn to phenomenological models to describe the hadronization process, i.e. how the quarks and gluons in the shower combine to form mesons and baryons. I will give a brief survey of three of the currently most popular descriptions.

The first picture, Local Parton-Hadron Duality (LPHD), is perhaps the simplest and comes from the realization that pQCD works well down to low scales. It assumes that each parton in the shower correspondes to one observable hadron. This is appealing in its simplicity and is what allows one to extrapolate the properties of the shower to the observed distibutions of real hadrons. In fact, it is more of a non-assumption of the hadronization proccess than an assumption, a sort of "simplest case" scenario for hadronization, making no distinction between the formation of baryons and mesons. It assumes that creation of particles and resonance decays have little effect on the event properties, causing at most a slight correction to the predicted distributions. This leads into to the concept of "soft confinement", i.e. that the process of confining quarks in hadrons takes place at a low energy scale, and of *localized hadronization*, i.e. that the

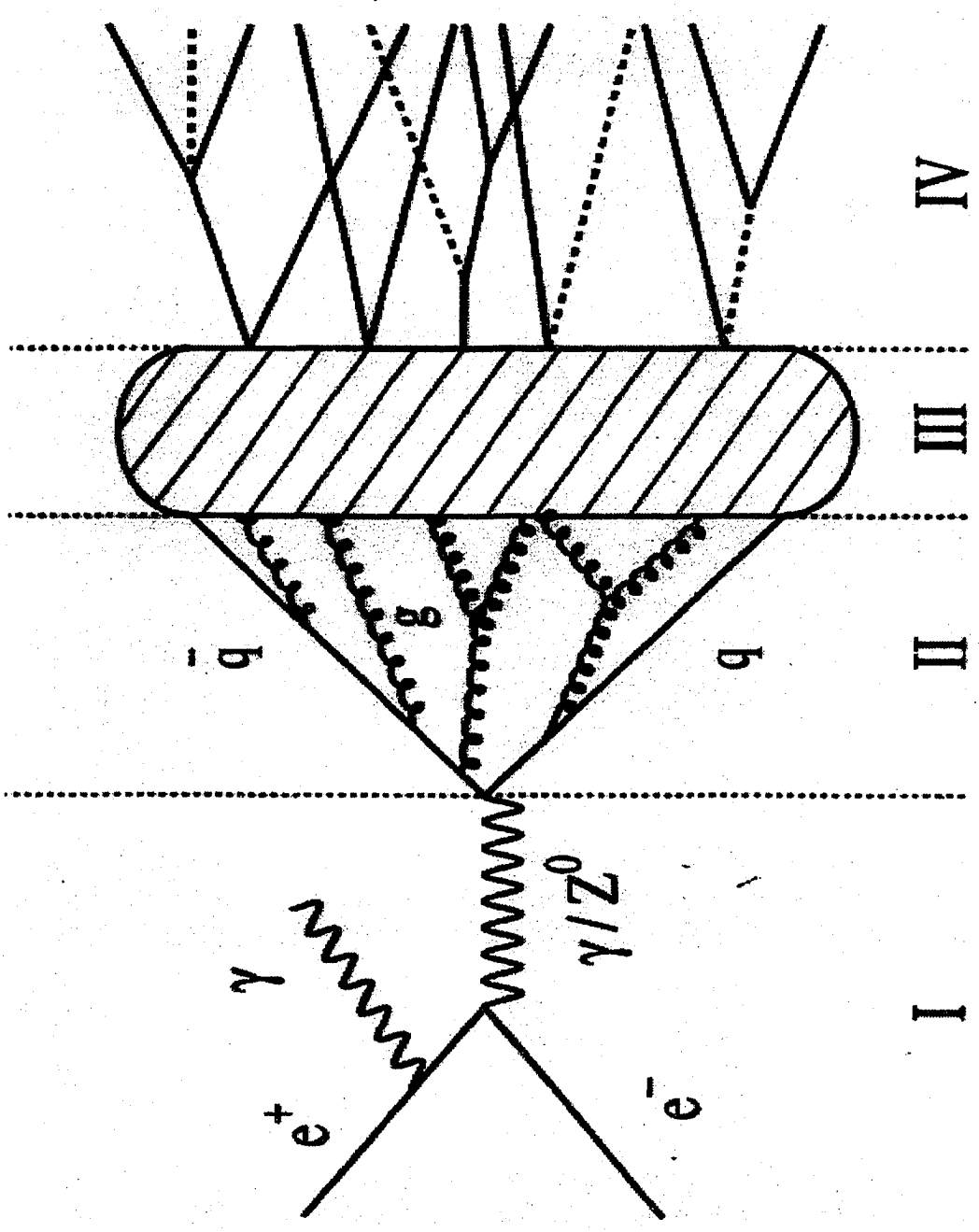

Figure 2.9 Representation of the stages in $e^+e^- \rightarrow$ *hadrons*: I) electroweak phase, II) parton shower, III) hadronization, and IV) final state hadrons. Phase III, hadronization, defies explanation by current theories, thus one must resort to phenomenological models to explain what happens here.

formation of hadrons proceeds locally, involving at most only a few neighboring partons.

Another popular model is the string model, particularly the one from Lund which has been implemented into the JETSET Monte Carlo simulation [18]. As the primary quarks separate, the color field can be interpreted as a narrow tube of force between the quarks. This narrow tube, with transverse dimensions on the order of 1fm, can be interpreted as a string which is terminated at the ends by the quark and anti-quark. As the quarks separate, the string stretches like a rubber band being pulled apart, the energy density increases and it becomes energetically favorable (and quantum mechanically possible) for the string to break, forming a quark-anti-quark pair ($q\overline{q}$) or a diquark-anti-diquark pair ($(q\overline{q'})(\overline{q}q')$), so that now there are two string pieces termined by quarks and diquarks. This process repeats until there is not enough energy left to break the strings. These remaining pieces of string, terminated by quarks and diquarks, are taken to be the final state hadrons.

Alternatively, in the HERWIG model [19] the secondary quarks remaining at the end of the parton shower are grouped into clusters. Any remaining gluons are forced to form a pair of light quarks (u or d) before the clustering process. These clusters then decay. The decays are governed purely by kinematics and statistics. (HERWIG is an acronym coming from the fact that it is a Monte Carlo event generator for simulating "Hadron Emisson Reactions With Interfering Gluons".)

To obtain a better understanding of the hadronization process, one must turn to experiment to gather more clues as to the subtler mechanics of hadron formation. One way to do this is to compare the fragmentation properties of quark jets and gluon jets. Since gluons couple more readily to gluons, one might expect to find a difference in hadron production in each type of jet. Previous studies [21, 23, 28] have measured production of the scalar mesons π, $K^{\pm}$, K^0 and the baryons p, Λ^0. Additional measurement of other identified particles need to be made since their production mechanisms may be different. It is this need which motivates the present analysis of ϕ and K^{0*} produced at LEP.

CHAPTER 3 LEP AND DELPHI

3.1 LEP Collider

The Large Electron-Positron collider (LEP) at the European Laboratory for Particle Physics (CERN) is a high energy particle accelerator used to study electroweak physics. At LEP it is possible to study both the weak interaction, via Z^0 and $W^{\pm}$ production, and Quantum Chromodynamics (QCD) via hadron production. In fact, being an electron-positron collider, LEP is an excellent laboratory for study of these processes because it is devoid of hadronic beam fragments and the high multiplicities present in hadron-hadron colliders. The data used in this analysis was taken at LEP.

CERN is located on the French-Swiss border near Geneva, Switzerland. The LEP ring, which is 26.7km in circumference and actually crosses the border, sits in a 3.8m diameter tunnel 50-170m below the surface of the earth (Figure 3.1). LEP is a particle accelerator consisting of an evacuated beam pipe, 3392 dipole magnets, 876 quadrupole magnets, 520 sextupole magnets, and 128 radio-frequency acceleration cavities. Electron and positron beams circulate around the ring in opposite directions and are allowed to collide at each of four experiments: DELPHI, ALEPH, OPAL, and L3. During the data collection period used here (LEP I), each beam had an energy of about 45.6GeV which together add up to the mass of the Z^0 at 91.2GeV. LEP was built to run at this energy specifically to study the Standard Model at the Z^0 mass. At the Z^0 resonance, the electron-positron cross section increases dramatically (see Figure 3.2).

Production of the electrons and positrons for LEP begins with the appropriately-

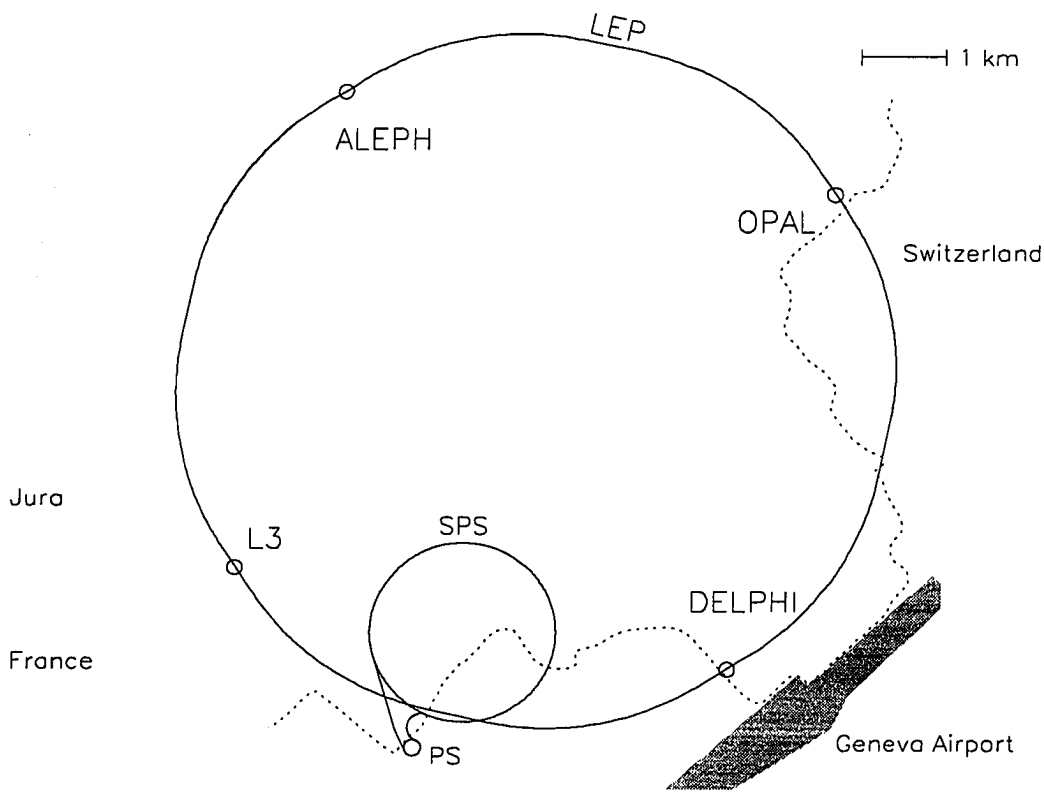

Figure 3.1 The Large Electron-Positron collider (LEP) at CERN.

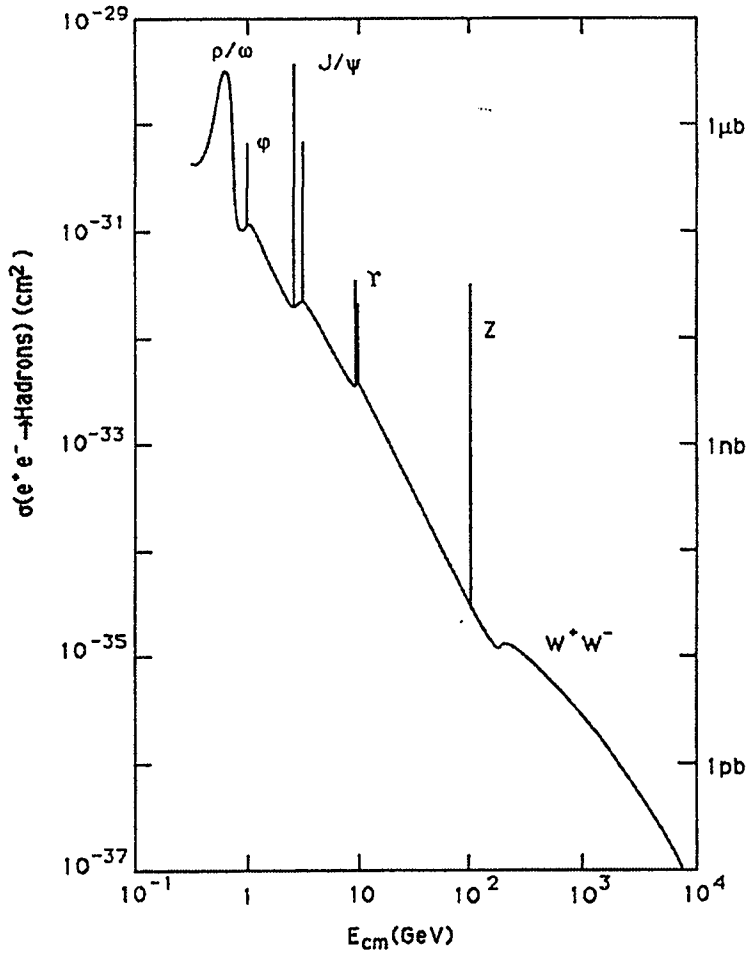

Figure 3.2 Cross section for $e^+e^- \to$ *hadrons* as a function of energy [35].

named LEP Injection Linacs (LIL) (Figure 3.3). Electrons are created by an electron gun and accelerated to 200MeV. Part of the electron beam is collided with a high-Z target to produce 10MeV positrons, which are then also accelerated to 200MeV. From here the beams are collected in the Electron-Positron Accumulator (EPA) until a sufficient beam current has been reached. Next, the beams are sent to the Proton Synchrotron (PS) and accelerated to 3.5GeV before being passed to the Super Proton Synchrotron (SPS) where they are accelerated to 20GeV.

The beams are finally injected into LEP and accelerated to their final energy of 45.6GeV. Each beam is concentrated in bunches about 2cm long with cross-sectional dimensions of $\sigma_x \approx 200\mu$m and $\sigma_y \approx 8\mu$m [36]. Each bunch contains roughly 2.5×10^{11} particles. In 1993 LEP began running with 8 bunches in each beam. Starting in 1996, LEP was upgraded with superconducting radio-frequency cavities to run at higher energies in order to pass the $W^{\pm}W^{\mp}$ threshold at 160.44GeV in what is referred to as LEP II. The analysis presented in this thesis is based on data taken during the running at the Z^0 production peak, i.e. LEP I.

Luminosity is defined $\mathcal{L} = \frac{n}{\sigma}$, where n=number of events/second and σ=cross-section. For colliding beams, in this case an electron beam against a positron beam, the luminosity can be written as

$$\mathcal{L} = \frac{\mathrm{N}^+ \cdot \mathrm{N}^- \cdot k \cdot f}{4\pi \cdot \sigma_x \cdot \sigma_y}$$

where $\mathrm{N}^{\pm}$ = number of e^+ or e^- in a bunch, k = number of bunches, f = revolution frequency of the beams, and σ_x,σ_y = the transverse beam dimensions. In 1994 the luminosity was about $2.2 \times 10^{33}\mathrm{cm}^{-2}\mathrm{s}^{-1}$.

The current of each beam is given by

$$\mathrm{I} = \mathrm{N}^{\pm} \cdot k \cdot f \cdot e^{\pm}$$

where $e^{\pm}$ is the elementary charge on the electron/positron. Typical beam currents at LEP are on the order of 1.5mA. By comparison, the current in a common 3 volt

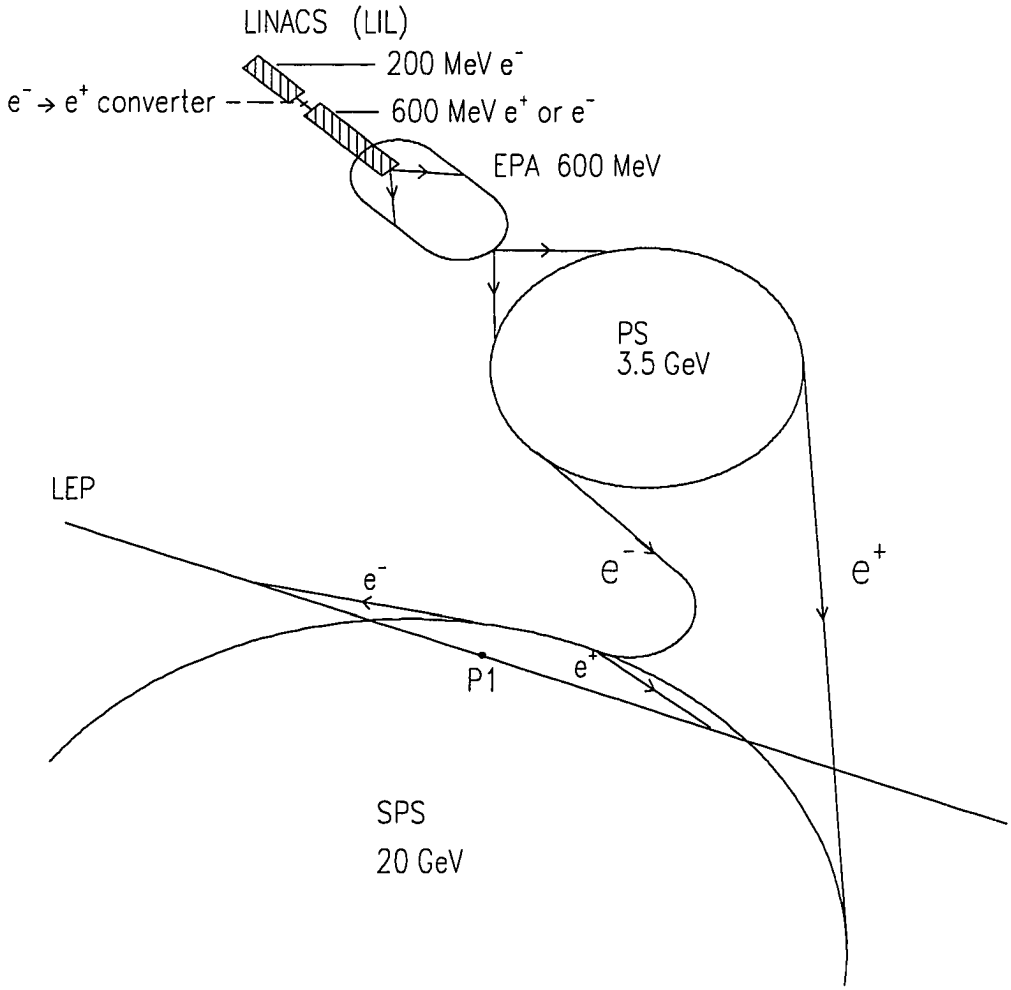

Figure 3.3 The accelerators used to inject LEP with electrons and positrons.

flashlight is on the order of 300mA [37]. Of course the energy of the electrons flowing in the flashlight is only 3eV whereas the energy of the electrons in LEP is 45.6MeV.

It takes roughly half an hour to fill LEP and accelerate the beams to the final energy. The beam currents decrease over time due to beam-beam interactions, synchrotron radiation, and beam-gas interactions. After about 10-12 hours, the currents have dropped so low that LEP is refilled with a new batch of electrons and positrons.

3.2 DELPHI Detector

DELPHI is an acronym for DEtector with Lepton, Photon, and Hadron Identification. It was constructed during a 7 year period from 1982 to 1989 at a cost of 150 million Swiss francs. At present the international collaboration is comprised of more than 600 physicists and technicians from 52 institutions.

The DELPHI detector (Figures 3.4, 3.5, and 3.6) is located in an underground cavern 100 meters below the surface. It is a 4π detector composed of a cylindrical barrel region sealed by two end caps and is self-shielding, allowing access to the cavern even while the beam is on and the experiment is taking data. The detector is 10 meters in diameter, over 10 meters long, and weighs more then 3500 metric tons. Read-out electronics are housed in four three-story barracks. From here, data is shipped to the control room on the surface via ethernet and a fiber optic cable.

In analyzing data collected by DELPHI, we use a right-handed coordinate system in which the z-axis lies in the direction of the electron beam, the y-axis points up and, therefore, the x-axis points in toward the center of LEP. The corresponding cylindrical coordinate system has r as the radial distance from the z-axis and ϕ is the angle in the xy-plane as measured from the x-axis. An additional angle, θ is defined such that $\theta = \arctan(r/z)$. The origin of the coordinate system lies in the center of the detector at the e^+e^- interaction point.

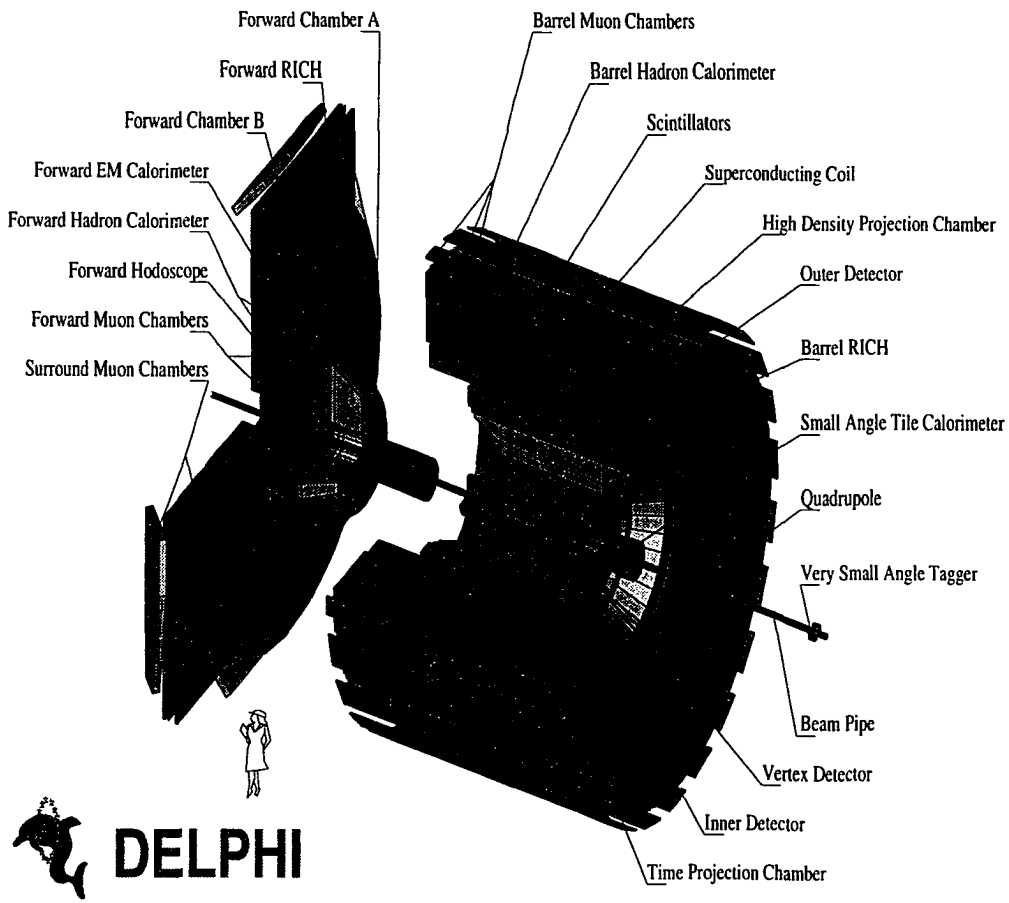

Figure 3.4 The DELPHI detector.

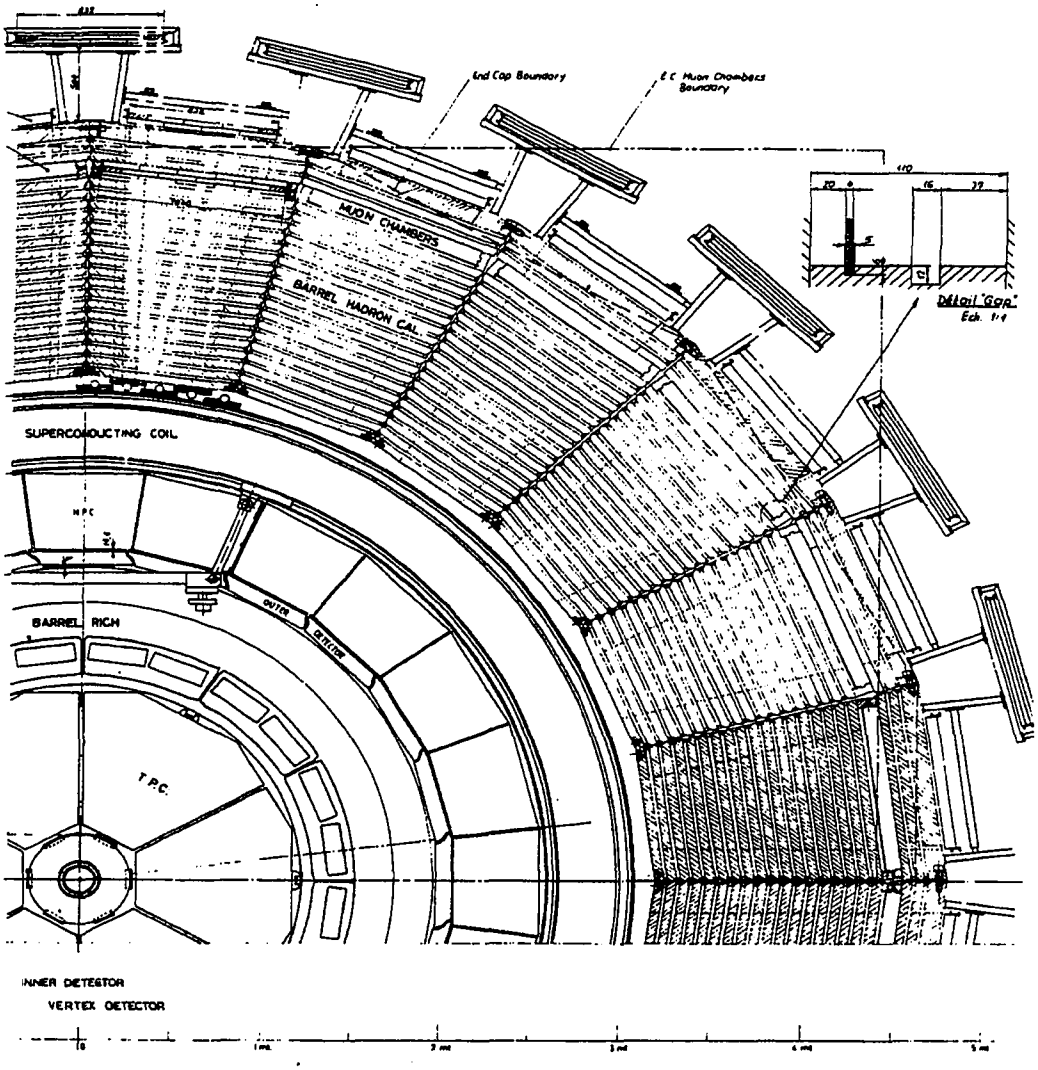

Figure 3.5 End view schematic of the DELPHI detector [38].

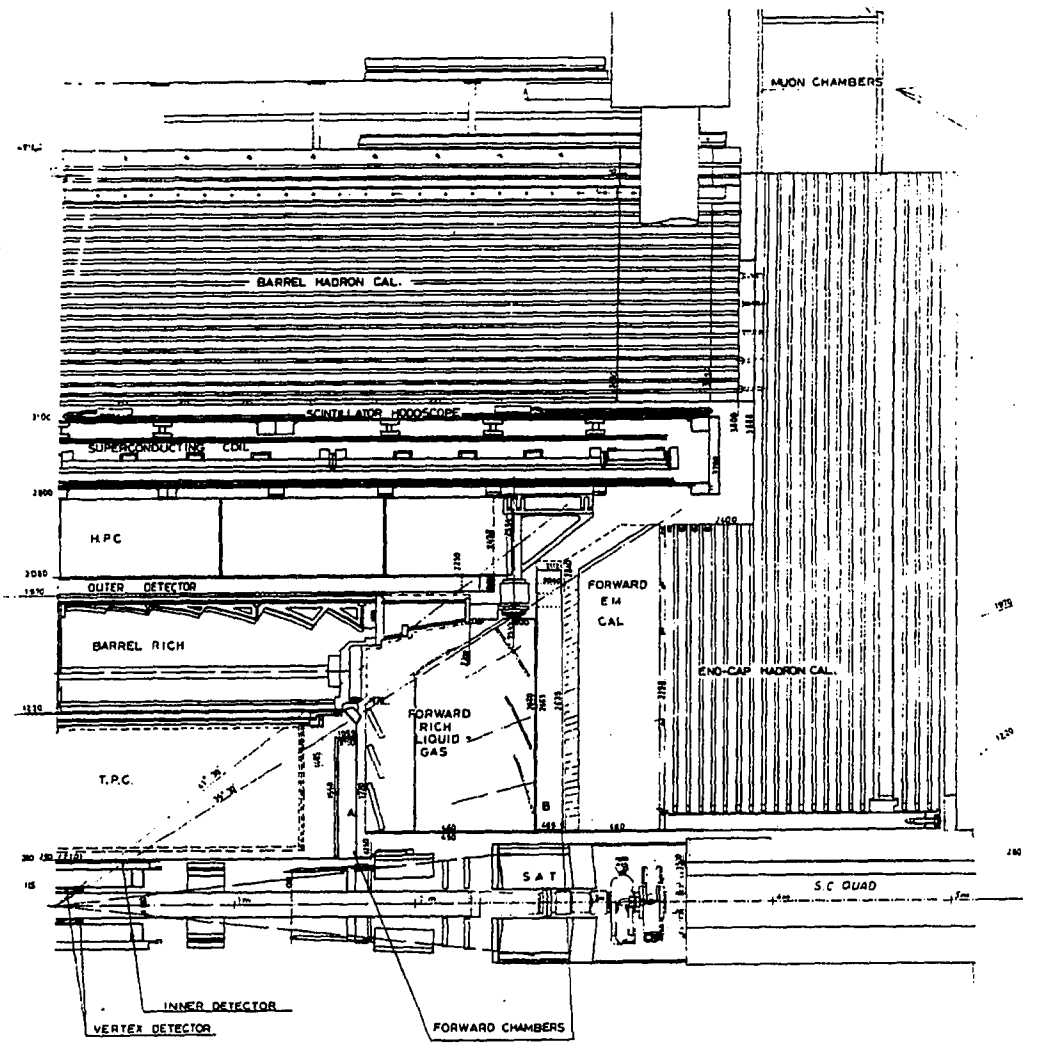

Figure 3.6 Side view schematic of the DELPHI detector [38].

3.2.1 Tracking

Tracking is accomplished with the VD, ID, TPC, and OD in combination with the curvature of the tracks in the magnetic field produced by the solenoid.

Solenoid The magnetic field in the central part of the DELPHI detector is produced by the world's largest superconducting coil. The solenoid is made of copper-packed Ni-Ti filaments cooled to T=4.7K by a forced flow of liquid helium. A current of 5000A creates a magnetic field of 1.2T.

The momentum of particles in DELPHI is determined by measuring the curvature of their trajectory in this magnetic field according to the relation

$$R = \frac{p}{qB}$$

where R is the radius of curvature, p is the momentum, q is the charge, and B is the magnetic field. The magnetic field also reduces transverse dispersion in drift devices such as the TPC and HPC by virtue of the fact that the ionization is drifted parallel to the magnetic field, so any motion transverse to the field is translated into helical motion by the force of the magnetic field on the drifted charge, $\mathbf{F} = q\mathbf{V} \times \mathbf{B}$.

3.2.1.1 VD - Vertex Detector

Description The Vertex Detector (VD) consists of three layers of silicon microstrip detectors located at distances of 6.3, 9.0, and 10.9cm from the beam axis covering polar angles from $44° \leq \theta \leq 136°$. Each layer has 24 modules with 10% overlap to provide complete coverage in ϕ. In 1994 the first (Closer) and third (Outer) layers were equipped with double-sided microstrip layers to provide both $r\phi$ and z measurements.

Performance The resolution is $\sigma(r\phi) = 7.6\mu$m and $\sigma(z) = 9\mu$m (for particles passing perpendicularly through the layers; this is smeared out for particles passing at

Table 3.1 Detector resolutions

Detector	$\sigma(r\phi)$	$\sigma(z)$	$\sigma(\phi)$	Δz	two track sep
VD	7.6μm	9μm			
ID	50μm		1.5mrad	0.5mm	1mm
TPC	250μm	900μm			1.5cm
OD	110μm	3.5m			

an angle, i.e. $\theta \neq 0$).

3.2.1.2 ID - Inner Detector

Description The Inner Detector (ID) is a drift chamber with jet-chamber geometry comprised of 24 azimuthal sectors providing up to 24 $r\phi$ points per track between radii of 12-23cm. Tracks between polar angles $23° \leq \theta \leq 157°$ cross at least 10 wires. Surrounding the jet-chambers are 5 cylindrical MWPC layers used for triggering and for resolving left-right ambiguities in the jet chambers.

Performance The ID provides single-track resolutions of $\sigma(r\phi) = 50\mu$m and $\sigma(\phi) = 1.5$mrad. The two-track separation resolution is 1mm. The z precision from a single MWPC layer is 0.5-1mm, depending on θ.

3.2.1.3 TPC - Time Projection Chamber

Description The Time Projection Chamber (TPC) is the primary tracking device in DELPHI. It is composed of two cylindrical chambers each 150cm long with inner and outer radii of 30cm and 120cm, respectively. Each chamber is divided into six sectors. A drift field is set up inside of the chamber so that ionization from a particle passing through the argon/methane gas (80%/20%) is drifted toward the end of the detector at a speed of 6.7cm/μs. At the end, the signal is read out via a system of 192 anode

wires and 1680 cathode pads in 16 circular pad rows. This gives a three-dimensional measurement of the particle's trajectory through the TPC.

Performance The spatial resolution is 250μm in the $r\phi$ plane and 900μm in z. The two-point resolution, i.e. the distance at which two tracks can be separated, is 1.5cm. The ionization loss of the particle can be sampled up to 192 times, the relative uncertainty being 6%. This provides particle identification for particles in the momentum range of a few hundred MeV up to 2GeV.

3.2.1.4 OD - Outer Detector

Description The Outer Detector (OD) consists of 5 layers of drift tubes located at radii of 197-206cm. Successive layer are staggered as are adjacent modules, thus providing complete azimuthal coverage. The OD covers polar angles in the range $42° \leq \theta \leq 138°$. Three layers are instrumented to measure the z coordinate of the track passing through the detector by timing the signal at both ends of the drift tube.

Performance The resolutions of the OD are $\sigma(r\phi) = 110\mu$m and $\sigma(z) = 3.5$cm.

3.2.2 Calorimeters

3.2.2.1 HPC - High-density Projection Chamber

Photon and electron identification is accomplished primarily by the High-density Projection Chamber (HPC). The HPC consists of 144 TPC-like modules but with layers of lead inside (Figure 3.7). Electrons and photons entering the HPC initiate electromagnetic showers, the energy and shape of which are sampled by drifting the ionization charge to detection pads at the ends of the modules. The modules are arranged in 6 rings of 24 modules each in a cylinder around the beam pipe with inner radius 208cm and outter radius of 260cm. The effective radiation depth of the HPC for a charged track

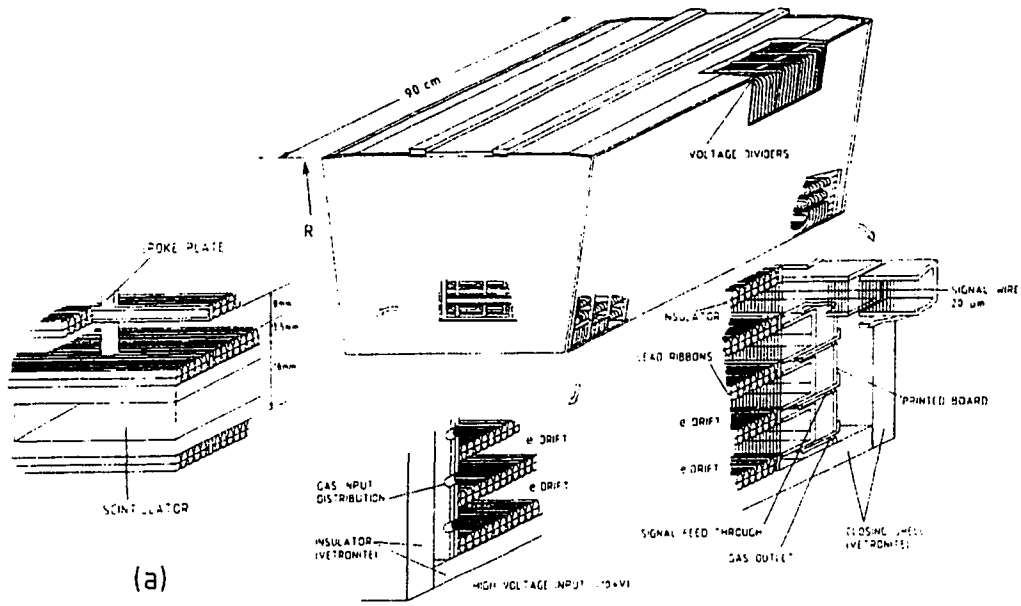

Figure 3.7 Sketch of one HPC module showing the layers of lead wiring inside [38].

passing through at an angle θ is $18X_0/\sin\theta$. The lead layers are electronically isolated lead wires which have a potential difference applied to form an electric field which drifts the ionization charge to the end of each module. At the end each module has 128 pads arranged in 9 rows along r. Pads are small toward the inner radius and get larger toward larger radii. This gives better energy resolution of the electromagnetic shower since it provides greater granularity around the region of maximum shower developement and more pick up area farther out where there is less energy deposition by the shower. The charge collected on each pad is read out in 256 time slots to determine the extent of the shower in z.

For 45GeV electrons, the z resolution σ(z) is 0.13cm, 0.22cm, and 0.31cm for the inner, middle, and outer rings, respectively. This gives a θ resolution of 0.6 mrad and a φ resolution of 3.1 mrad. The energy resolution of the HPC is 6.5% for 45 GeV electrons.

3.2.2.2 HAC - Hadron Calorimeter

The Hadron Calorimeter (HAC) is located outside the solenoid in the return yoke of the DELPHI detector and measures the energy of particles which initiate hadronic showers. It consists of 24 modules with more than 19,000 limited streamer tubes.

3.2.3 Particle Identification

Particle identification in DELPHI is accomplished using a combination of the identification capabilities of the numerous subdetectors. For charged tracks, this is primarily the dE/dx measurement from the TPC and the Cherenkov information from the RICH. Particles which shower in the HPC are either electrons or photons. Particles which shower in the HAC are primarily hadrons, while any particle which makes it to the MUON chambers is probably a muon.

3.2.3.1 TPC

As a charged particle passes through the TPC, it ionizes the gas. The amount of ionization depends on the charge, momentum, and mass of the particle. The sense wires in the TPC provide up to 192 ionization measurements per track. The dE/dx measurent allows separation of pions, kaons, and protons from about 200MeV up to nearly 2GeV. The top of Figure 3.8 shows monte carlo simulation of particle identification using the TPC.

3.2.3.2 RICH - Ring Imaging CHerenkov Detector

Description In addition to the measurement of ionization loss in the TPC, particle identification is provided by the Ring Imaging Cherenkov detector (RICH). When a charged particle travels through a dielectric medium faster than the speed of light in

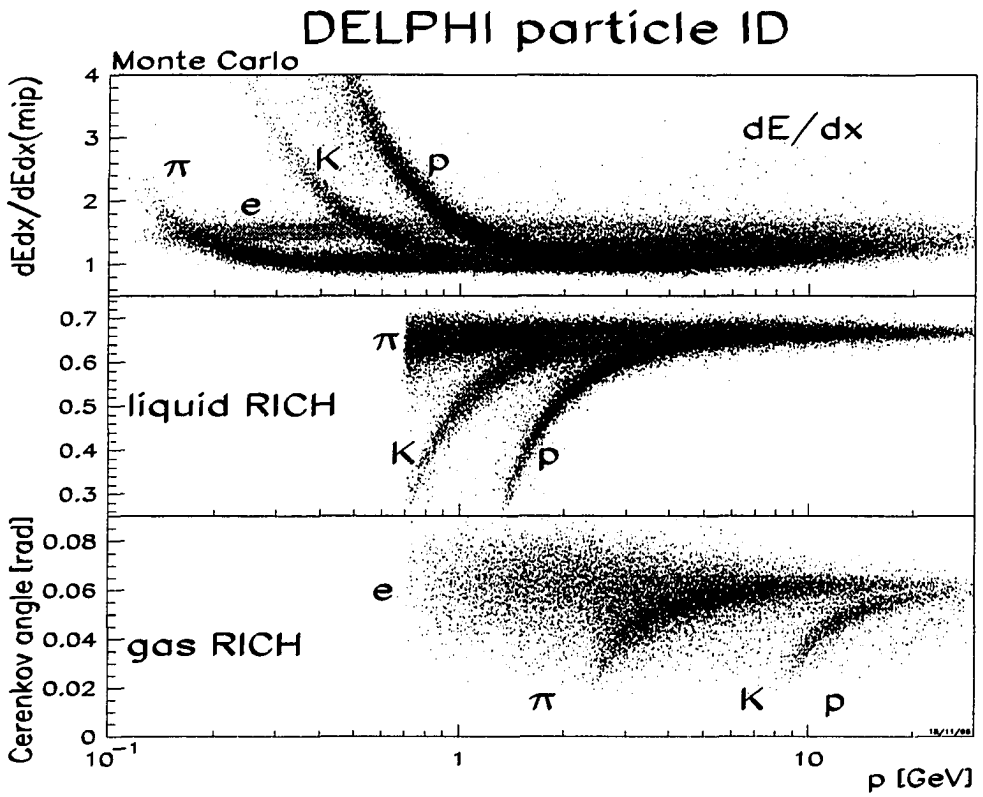

Figure 3.8 Monte Carlo simulation of DELPHI particle identification using dE/dx in the TPC and Cherenkov information from the RICHs.

that medium, it emits photons at an angle to its trajectory according to the relation

$$\cos\Theta_{CH} = \frac{\sqrt{1+m^2/p^2}}{\eta}$$

where $\cos\Theta_{CH}$ is the Cherenkov angle, m is the mass of the particle, p is the momentum of the particle, and η is the index of refraction of the medium. By knowing η and measuring Θ_{CH} and p, one can find the mass m. Besides measuring it directly, additional information on the angle is is given by the number of photons produced per unit length in the radiator medium which is proportional to $\sin^2\Theta_{CH}$. Figure 3.9 shows a schematic of the RICH detector. The radiators are perfluorocarbons which emit photons in the range 140-220nm. These photons are detected by a photosensitive time projection chamber (48 in barrel, 24 in each endcap).

Below a certain velocity, a particle of a given mass will not generate Cherenkov radiation. This is used to tag particles in what is called the "veto mode".

DELPHI has two RICH systems, one employing a liquid radiator and the other using gas, in order to identify particles over a wider momentum range than is possible with a single index of refraction. The liquid RICH provides particle identification from 0.7-4GeV while the gas RICH works from 2.5-25GeV. The bottom of Figure 3.8 shows monte carlo simulation of particle identification using the RICH systems.

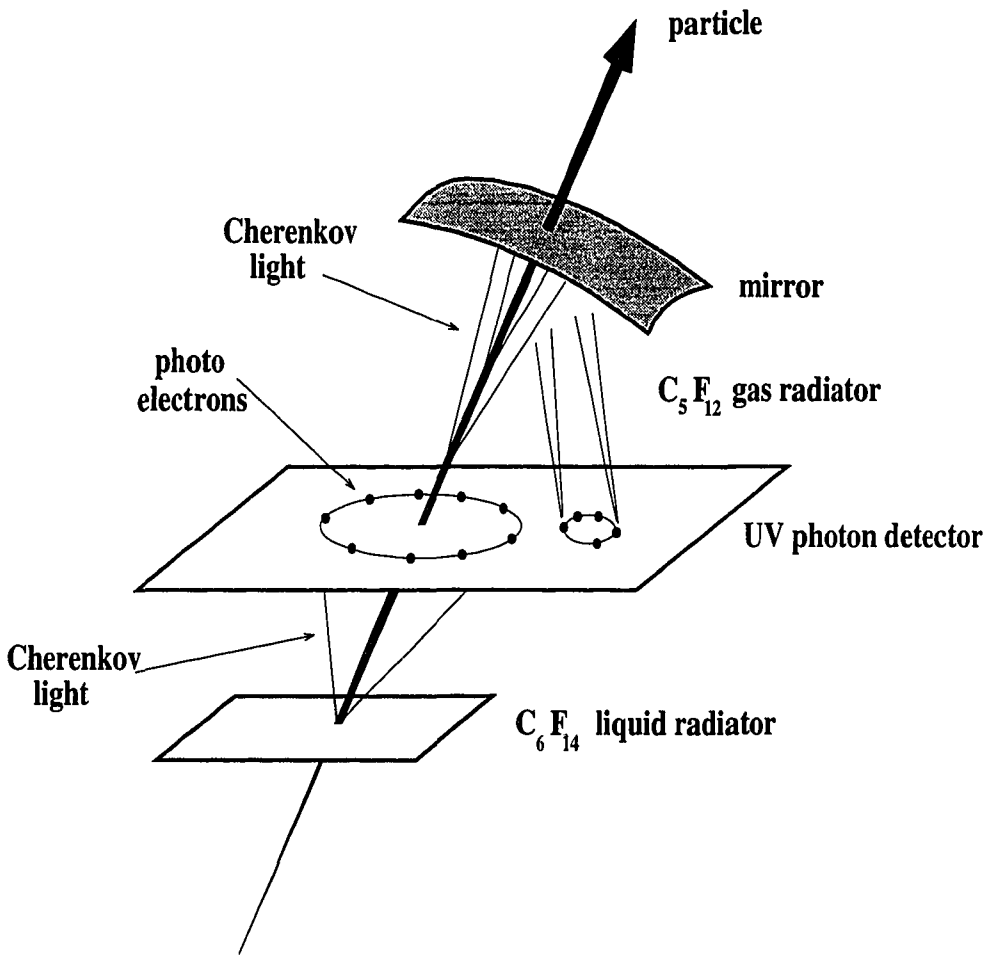

Figure 3.9 Schematic of the operation of the RICH detector.

CHAPTER 4 TRACK AND EVENT SELECTION

DELPHI data taken during 1994 was used in this analysis in order to take advantage of a fully operational RICH detector and an upgraded vertex detector [38]. Roughly 1400K hadronic events were used from the data recorded by DELPHI in 1994. An equivalent number of simulated Monte Carlo simulation events, hereafter referred to as "Monte Carlo events", was used to determine tagging efficiencies and provide background shape for subtraction from the data in order to extract a signal. The Monte Carlo used JETSET [18] to generate the primary physics which was then passed through the detector simulation DELSIM [39]. Real data events and Monte Carlo events were both passed through the DELPHI analysis program DELANA [40].

4.1 Track Selection

Tracks were selected using standard DELPHI criteria used to provide a sample of well-reconstructed tracks coming from the beam interaction point and to exclude tracks originating from beam gas interactions, cosmic rays, and secondary interactions in the detector. The cuts used are:

track momentum	$>$	0.4	GeV/c
relative error $\Delta E/E$	$<$	100	%
track length	$>$	30.0	cm
impact parameter R/Phi	$<$	4.0	cm
impact parameter Z	$<$	10.0	cm
polar angle θ	$>$	20.0	deg

These have been set to provide well-reconstructed tracks and are included in the standard DELPHI analysis software.

4.2 Event Cuts

Hadronic events were selected by requiring more than two non-collinear tracks in order to exclude $\ell^+\ell^-$ events, with an additional requirement of some minumum multiplicity to exclude $\tau^+\tau^-$ decays in which one or both of the τ's decays. There is also a requirement on the total visible energy so as to exclude $\gamma\gamma$ interactions. The following additional cuts were imposed to exclude τ events:

number of positive tracks	$\geq$	3
number of negative tracks	$\geq$	3
number of tracks	$\geq$	8
total energy	$\geq$	15.0 GeV

4.3 Jet Selection and Assignment

Three-jet events were selected using the DURHAM jet-finding algorithm [41]. This algorithm utilizes a scaled transverse momentum y_{ij} which is defined for each combination of particles,

$$y_{ij} = \frac{2 \cdot \min(E_i^2, E_j^2) \cdot (1 - \cos\alpha_{ij})}{E_{vis}^2}$$

where E_i and E_j are the energies of each particle (assuming the pion mass), α_{ij} is the angle between them, and E_{vis} is the visible energy in the event. The pair with the smallest y_{ij} is replaced by a pseudoparticle which is the vector sum of their momenta, y_{ij} is recalculated, and the process repeated. The algorithm is essentially building up jets of particles which are going in generally the same direction, each pseudo particle being a jet composed of two or more observed particles. This continues until there are no pairs with y_{ij} below some jet resolution value y_{cut}. The pseudoparticles remaining are considered to be jets. (The DURHAM algorithm is different from the JADE [42] algorithm in that it used scaled transverse momentum rather than the invariant mass of the pseudoparticle.) The number of jets found depends upon the choice is the resolution parameter y_{cut}. Figure 4.1 shows the number of 2-, 3-, and 4-jet events found as a function of y_{cut}. I chose a y_{cut} of 0.020 because it yields a reasonable sample of ≥ 3 jet events and this sample changes slowly as a function of y_{cut} around this value of y_{cut}. A good agreement is seen in the relative fraction of 2,3,etc.-jet events between real data events and simulated Monte Carlo events (see Figure 4.2). About 800,000 events, in both real data and Monte Carlo, were used to make the comparison.

Each jet was required to have a charged multiplicity greater than 1 and to have less than 85% of its energy coming from neutral particles in order to exclude photon jets and, thereby, $qq\gamma$ events.

To insure that each 3-jet event was a good, planar configuration of three jets, the sum of the angles between the jets had to add up to nearly 360°, i.e. $\theta_1 + \theta_2 + \theta_3 \geq 355°$, where θ_1 is the angle between jet 2 and jet 3, and so on. (See Figure 4.3.) Otherwise the event was discarded and not used in the analysis.

In order to compare particle production in gluon jets versus quark jets, it is necessary to determine which jet is the gluon jet. Hard gluons capable of forming isolated jets of hadrons are produced by bremsstrahlung radiation from quarks. These radiated gluons are usually lower in energy than the quarks that emit them (that is, lower than the

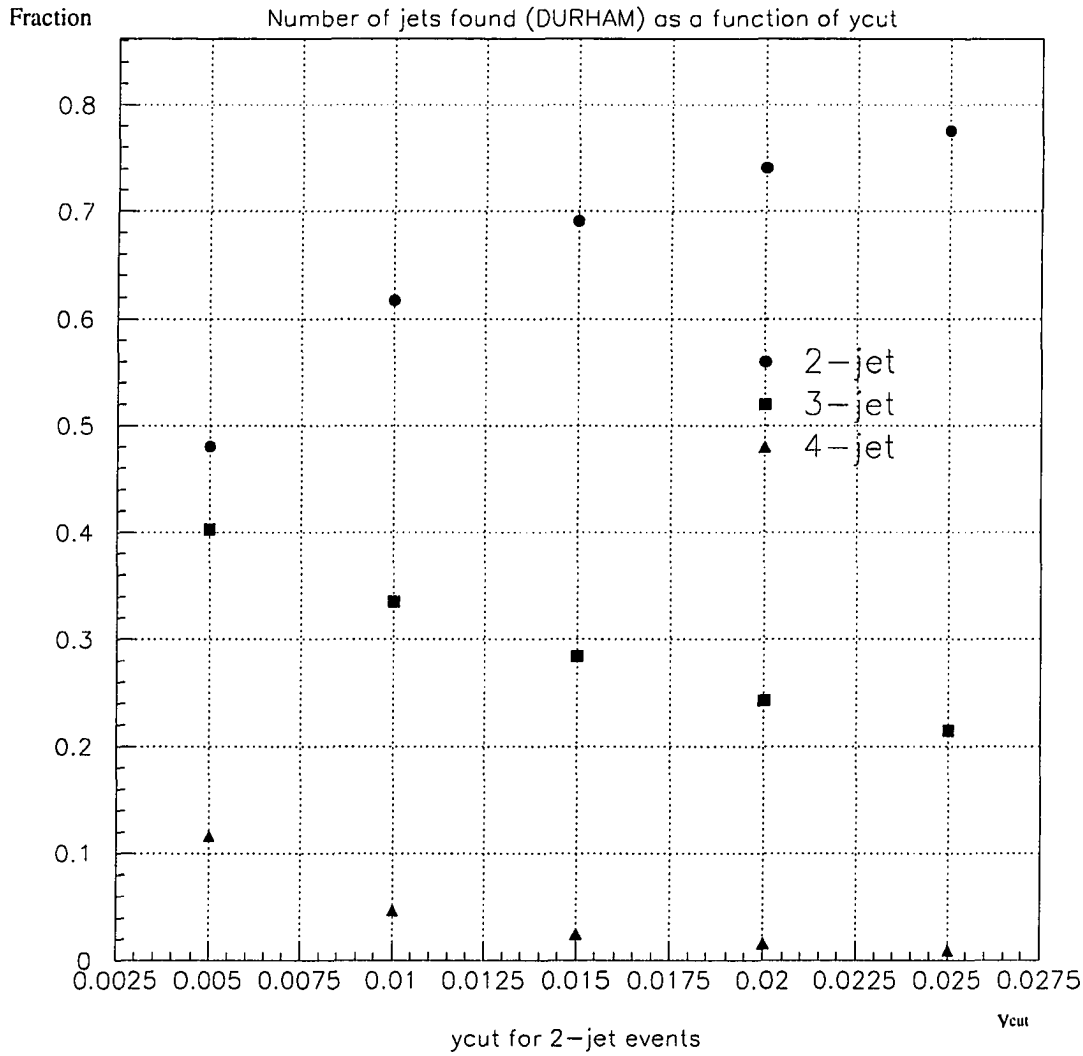

Figure 4.1 Number of jets found by the DURHAM algorithm as a function of y_{cut}.

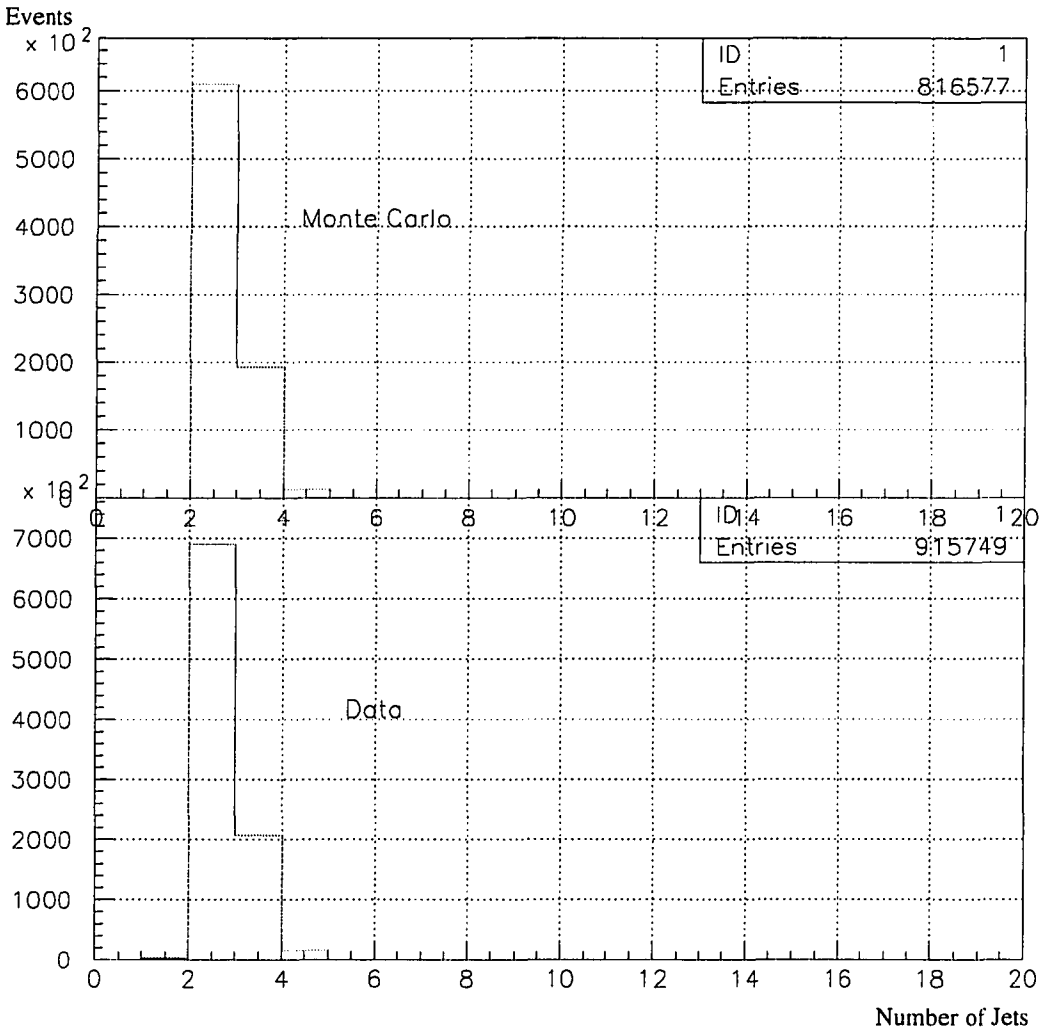

Figure 4.2 Number of jets using y_{cut}=0.020 for Monte Carlo events and real data. The key point here is that they agree, indicating that this is a reasonable y_{cut} value.

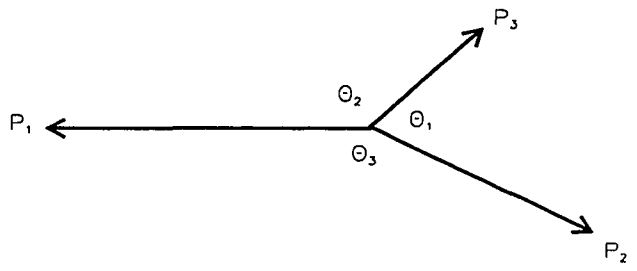

Figure 4.3 Definition of inter-jet angles θ_1, θ_2, and θ_3.

energy of the quark *after* radiation), thus the gluon jet is usually the least energetic jet, where the energy of a jet can be defined as the energy of all the particles associated with the jet.

However, rather than using the visible energy in each jet, one can use the angles between the jets and assume massless kinematics to calculate the energy of each jet in terms of the total available energy $\sqrt{s}$ (where $s^2 \equiv$ beam energy) and the angles between the jets. Since the lab frame is also the rest frame of the e^+e^- collision, the sum of the momenta of the jets must add up to zero. This means that the transverse momenta of two of the jets as measured with respect to the remaining jet must be equal in magnitude and opposite in direction (see Figure 4.4), so that

$$P_{2\perp} = P_{3\perp}$$

which can be rewritten

$$P_2 \sin\theta_3 = P_3 \sin\theta_2$$

which gives a relationship between the momenta for jets 2 and 3 in terms of the angles opposite each of them. If we assume massless quarks and qluons, which is reasonable at the energy scale of LEP I, we can subsititute $E_j = P_j$ to get

$$E_2 = E_3 \frac{\sin\theta_2}{\sin\theta_3}$$

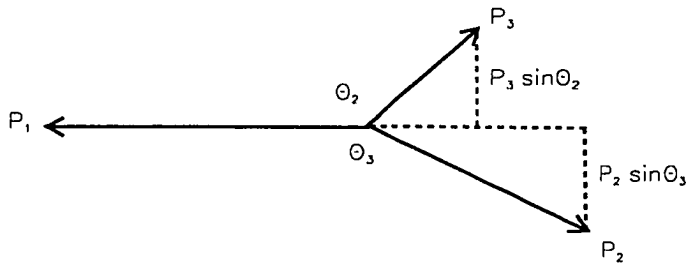

Figure 4.4 By momentum conservation, $P_i \sin\theta_j = P_j \sin\theta_i$.

or, more generally,

$$E_j = E_i \frac{\sin\theta_j}{\sin\theta_i}$$

between any two jets i and j. Next, by energy conservation, the total energy of all the jets must add up to the total available energy,

$$E_1 + E_2 + E_3 = \sqrt{s}$$

into which we can substitute the expression derived above relating jet energies and angles to get

$$E_1 \frac{\sin\theta_1}{\sin\theta_1} + E_1 \frac{\sin\theta_2}{\sin\theta_1} + E_1 \frac{\sin\theta_3}{\sin\theta_1} = \sqrt{s}$$

and rewriting,

$$E_1 = \left(\frac{\sin\theta_1}{\sin\theta_1 + \sin\theta_2 + \sin\theta_3}\right)(\sqrt{s})$$

for the energy of the first jet in terms of inter-jet angles and the collision energy. This relation holds for all three jets and can be rewritten in a more general form,

$$E_j^{calc} = \frac{\sin\theta_j}{\sin\theta_1 + \sin\theta_2 + \sin\theta_3}\sqrt{s}, \; j = 1,2,3$$

where, for example, θ_1 is the angle between jets 2 and 3.

For most sections of this analysis, it is sufficient to assign the least-energetic jet to the gluon. A quick study of Monte Carlo events confirmed that the most energetic jet

is associated with the primary quark which does not radiate a gluon. That means the two lower energy jets are associated with the other (radiating) quark and the gluon it radiated. Thus, it becomes a matter of choosing which of these two lower energy jets, jet 2 and jet 3, is the gluon. Figure 4.5 shows how often a "good tag" results when we naively assume that the lowest energy jet is associated with a gluon (as determined from monte carlo simulation, in which we can trace the decay chain of the partons down to observable particles). Taking the ratio of good tags to the total number of events we get the tagging efficiency, i.e. 37500/(37500 + 18000)=68%.

4.3.1 Additional Jet Cuts

Since the goal of this analysis is to compare particle production in quark jets versus gluon jets, it is necessary to select events which have a gluon jet in them. Three-jet events are also caused when there is a high-energy photon in the event. In order to exclude these $q\bar{q}\gamma$ events, each jet is required to have a particle multiplicity (number of particles) of at least 4. (The jet associated with the photon has a low multiplicity of only one or, at most, a few particles.) This left only those 3-jet events from $q\bar{q}g$.

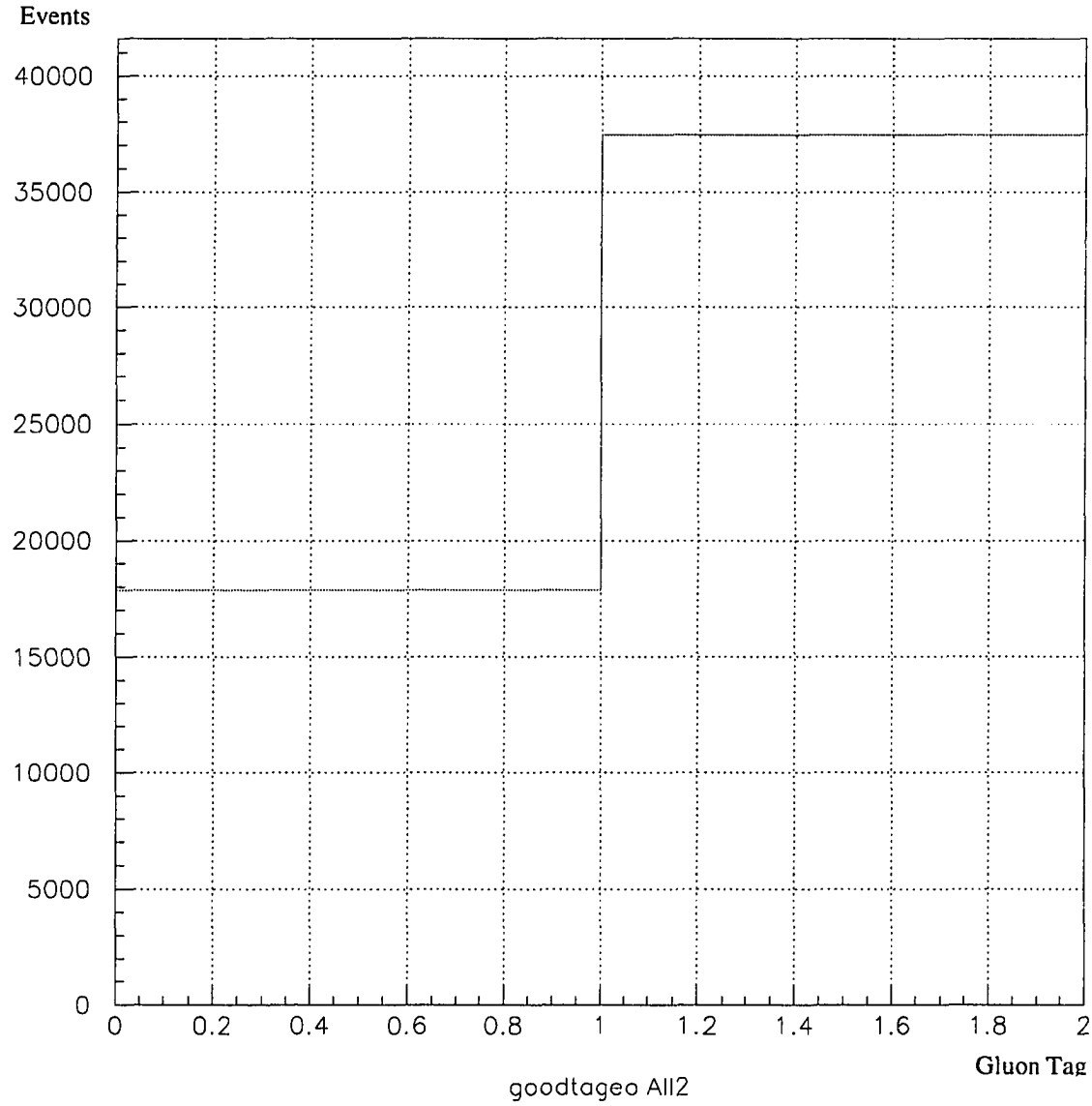

Figure 4.5 Good tagging of the gluon jet by assigning it to the lowest energy jet (1=good tag, 0=bad tag).

CHAPTER 5 RESONANCE ANALYSIS

5.1 Resonance Reconstruction

Having determined a way of assigning jets as coming from quarks or gluons, we can now move on to comparing particle production in each type of jet. Previous studies have done this for charged particles and long lifetime two-particle-decay particles like the K^0 and Λ^0. However, particles which decay essentially at the interaction point are much more difficult to measure because their decay products are buried in a large background of particles produced in the string fragmentation. The resulting combinatorial background is horrendous.

Resonances are reconstructed experimentally by taking particles observered in the detector and combining them into a candidate resonance. These are referred to as "candidates" because there is no way to tell, a priori, if all the particles being combined came from the same decaying resonance or not. Only by plotting the masses of all the candidates does one see the resonance, i.e. as a peak sitting on top of some background.

A number of resonances were searched for in this analysis and a summary is given in Table 5.1. Several could not be reconstructed because either the signal was too weak or the combinatorial background was too large. Due to the fact that there are so many pions produced in a hadronic event at LEP, any combination which includes pions will have a large background. Likewise, any combination which uses photons has to contend with the large number of photons in such an event, many of which come from the decay $\pi^0 \to \gamma\gamma$. On that note, any decay with a π^0 in it is subject to a large background due

Table 5.1 Resonances searched for in this analysis. Only the ρ, K^{*0}, and ϕ showed a signal above background. Of these three, only the latter two were sufficiently distinct to be used for making measurements.

Resonance	Search result
$\eta(547) \rightarrow \gamma\gamma$	not seen
$\eta(547) \rightarrow \pi^+\pi^-\pi^0$	not seen
$\rho(770) \rightarrow \pi^+\pi^-$	barely seen
$\omega(782) \rightarrow \pi^+\pi^-\pi^0$	not seen
$K^{*0}(892) \rightarrow K^+\pi^-$	seen
$\eta'(985) \rightarrow \pi^+\pi^-\eta$	not seen
$\phi(1020) \rightarrow K^+K^-$	seen

to the fact that there are many false π^0s being included in the reconstruction. In the case of the $\eta' \rightarrow \pi^+\pi^-\eta$, additional restraints were made on the mass of the η which goes to $\pi^+\pi^-\pi^0$ and should be quite narrow, but even this didn't reveal the η'.

The only practical solution is to look for particles which decay to one or more kaons. The reason for this is that by identifying kaons it is possible to reject much of the pion background. The effect of identifying kaons can be seen by comparing the mass plots for $\rho \rightarrow \pi^+\pi^-$, $K^{*0} \rightarrow K^+\pi^-$, and $\phi \rightarrow K^+K^-$ which involve 0, 1, and 2 kaons in the reconstruction, respectively (Figure 5.1).

While it would have been nice to have done this analysis using many resonances, the particle multiplicity in hadronic events at LEP and the difficulty of reconstructing three-body decay modes conspired against observing most of the resonances sought for. Only the K^{*0} and ϕ were high enough above background to be used to compare their production in quark and gluon jets.

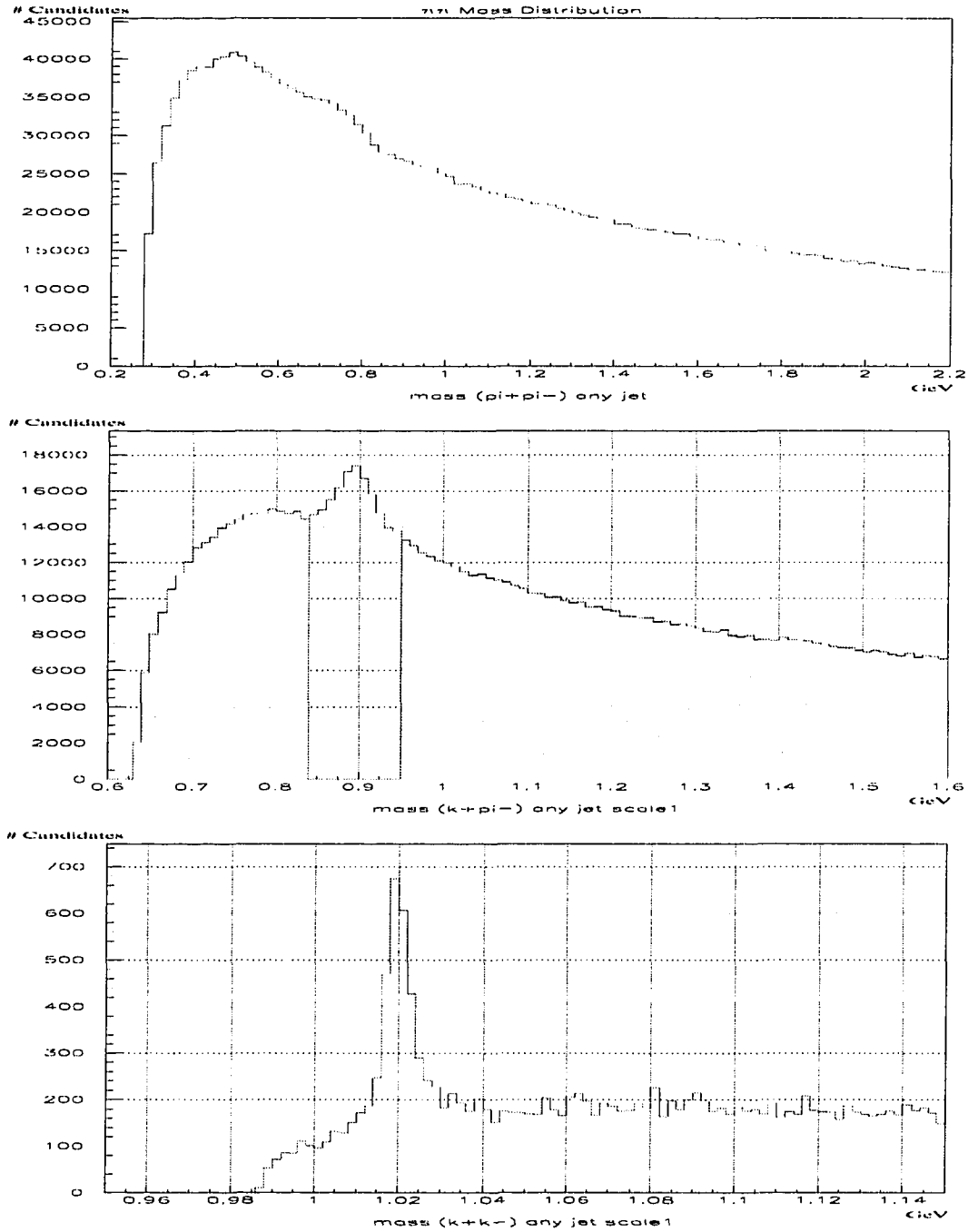

Figure 5.1 Mass plots for $\pi^+\pi^-$, $K^+\pi^-$, and K^+K^- in which one can see the effect of background reduction that comes from identifying 0, 1, and 2 kaons, respectively. In the first plot, the ρ is nothing more than a bump on the background, whereas in the next two plots the K^{*0} and ϕ are easily seen.

5.2 $\phi \rightarrow K^+K^-$ Analysis

The first resonance we will discuss will be the ϕ in the decay mode $\phi \rightarrow K^+K^-$ because it is easiest to measure due to its narrow width and the backround can be reduced by virtue of DELPHI's unique ability to identify kaons over a wide momentum range. Kaons are identified using combined information from the liquid RICH, gas RICH, and the TPC. Pairs of kaons assigned to the same jet, each kaon being required to pass the standard cut for the combined tag, were put together to form ϕ candidates (see Figure 5.2). Of these, only those with a combined mass within 50MeV of the ϕ mass were used in order to exclude most of the background. The amount of false ϕ candidates can be determined by fitting the background under the ϕ peak in the K^+K^- spectrum, but the shape of this false signal in the ζ and P_T measurement can only be determined from Monte Carlo simulations.

5.2.1 Scaled Longitudinal Momentum ζ

The longitudinal momentum of the ϕ candidate scaled to the jet energy, $\zeta \equiv p_{\parallel}/E_{jet}^{calc}$, gives some indication of how much the ϕ candidate is a leading particle in the jet. This is essentially the momentum fraction carried by the ϕ but normalized to the jet energy rather than the jet momentum due to the fact that gluon jets are broader than quark jets of the same energy, which would shift the momentum fraction to higher values. Figure 5.3 shows the ζ distrubution for the ϕ candidates. Data is represented by points and the Monte Carlo by a solid line. The dashed line represents the non-ϕ (determined from Monte Carlo by plotting ϕ candidates made of kaons who, in the simulation, do not have the same parent which is also a ϕ) and the shaded histogram shows the result of subtracting this background from the data, i.e. the shaded area should represent the "true" distribution.

Comparing the shaded distribution for the slower quark jet and the gluon jet it

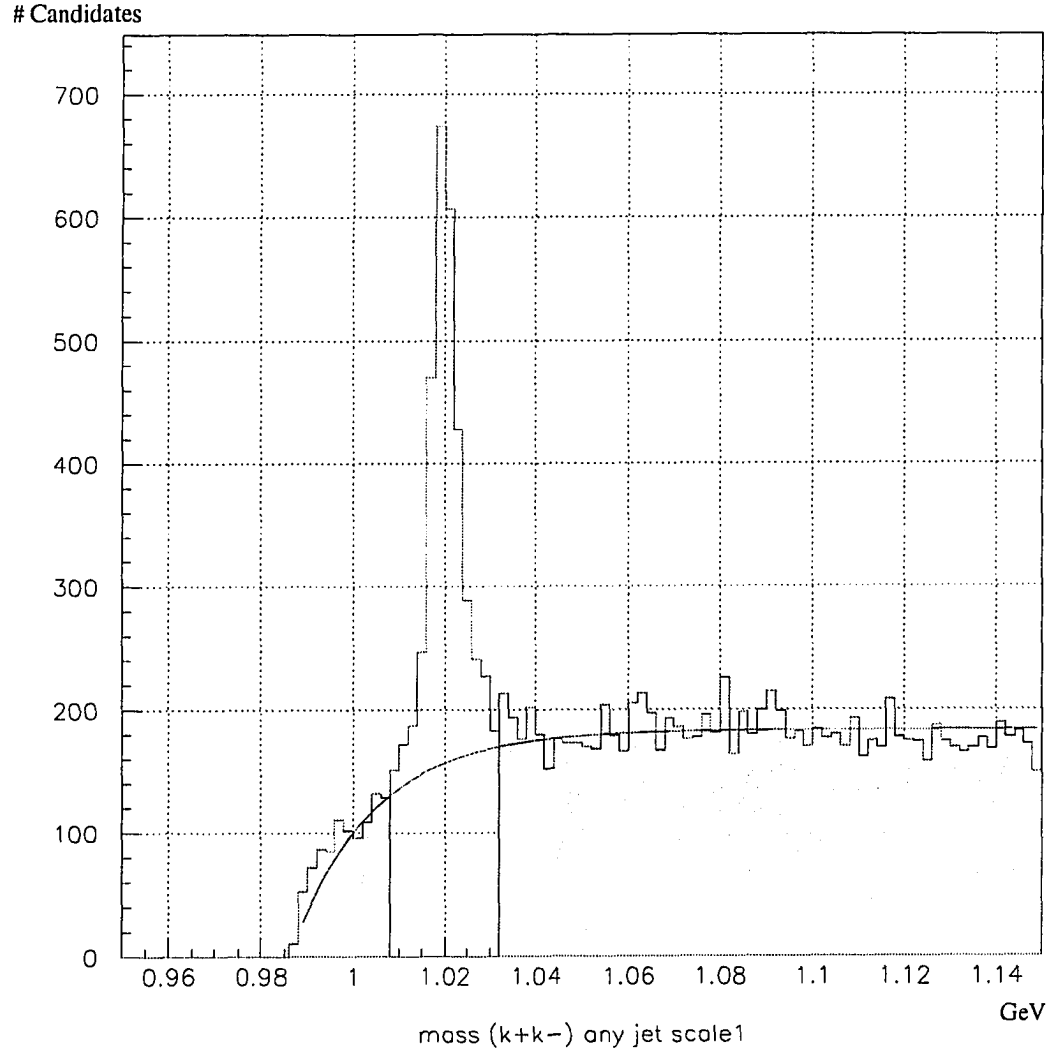

Figure 5.2 K^+K^- invariant mass spectrum showing the prominent ϕ peak. The unshaded region indicates kaon pairs considered as ϕ candidates.

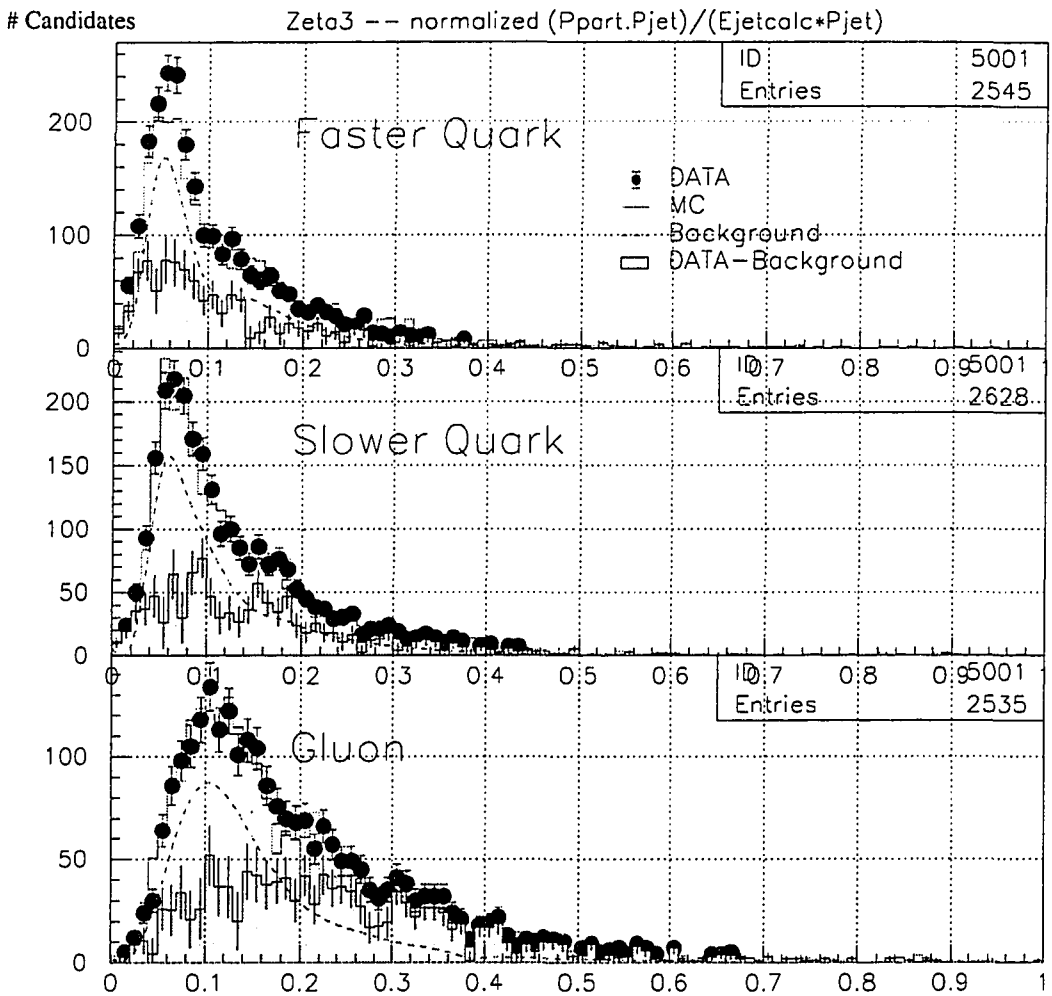

Figure 5.3 ζ, the ϕ longitudinal momentum normalized to jet momentum.

seems that the fractional longitudinal momentum carried by ϕ produced in gluon jets is slightly harder than for those produced in quark jets. If true, one has to wonder why. One interesting possibility is that the ϕ (and other isoscalar states, η, η', ω) may contain a significant gg component and, therefore, might appear more often as leading particles in gluon jets [6]. However, an investigation of the relative shapes of single particle distributions in Monte Carlo and real data shows that they peak more sharply in Monte Carlo, which explains why the "true" distribution seems harder. In fact, it is not a "true" distribution because the Monte Carlo does not accurately reproduce the particle distributions measured in data, i.e. when we subtract the background shape determined from Monte Carlo from the data, we find that the Monte Carlo background is artificially too low at higher momenta, resulting in an enhanced "signal". Thus, it is not possible to say from this that the ϕ tends to be produced as a leading particle in gluon jets. Another clue that nothing abnormal is going on with the ϕ production is to note that, without doing this subtraction, the data and Monte Carlo distributions match extremely well, i.e. the Monte Carlo actually does a good job of reproducing the data overall. Getting Monte Carlo simulations to accurately match data when one is dealing with complex, highly inhomogeneous detectors like DELPHI is a difficult and ongoing task. There are always discrepancies between the two and one must watch out for them.

Plotting the longitudinal momentum without first normalizing to the jet energy yields a plot (Figure 5.4) which is qualitatively similar except that the harder "true" spectrum in the gluon plot is not as apparent.

5.2.2 Transverse Momentum P_T

The transverse momentum, P_T, of particles produced in fragmentation is another hypothesized difference between quark jets and gluon jets which has yet to be measured by many experiments for the ϕ. Figure 5.5 shows the p_T distribution for ϕ candidates

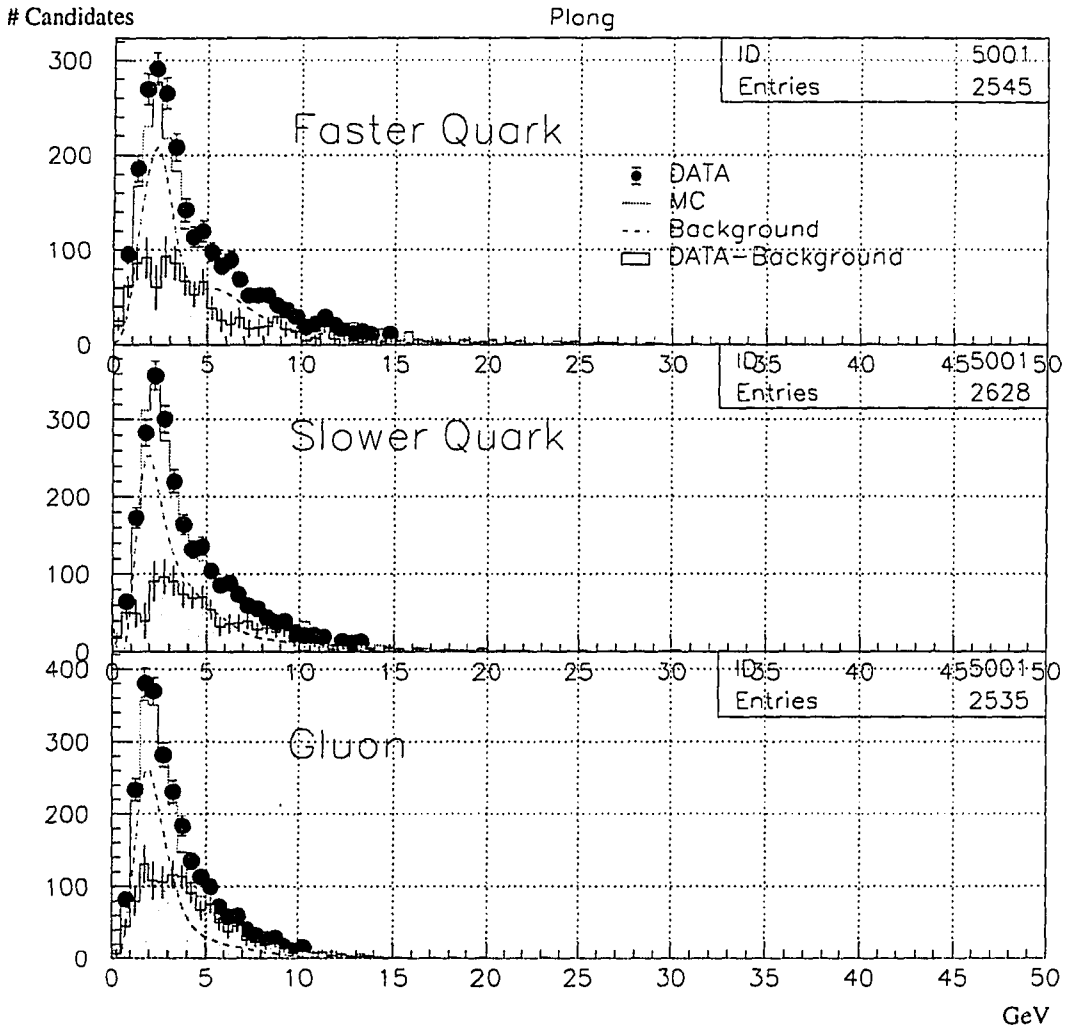

Figure 5.4 ϕ longitudinal momentum (unnormalized).

in quark jets and gluon jets. The P_T distribution of ϕ seems to be the same in quark and gluon jets.

5.2.3 Transverse Momentum Out of the Event Plane P_{T-out}

Another useful measurement is the component of the transverse momentum lying out of the event plane, P_{T-out}. This may be a more sensitive probe of the true P_T characteristics of hadronization than a measurement of the total observable P_T. The latter may be dependent on or affected by the transverse momentum of the gluon jet and the angles between it and the quark jets. Another way to say it is that the high P_T of the gluon can hide the soft P_T effects of the hadronization process. Figure 5.6 shows the P_{T-out} distribution for ϕ candidates in quark jets and gluon jets.

5.2.4 ϕ Analysis Summary

Making ϕ candidates from K^+K^- pairs and measuring scaled longitudinal momentum ζ, transverse momentum P_T, and transverse momentum out of the event plane P_{T-out} showed that distributions in real data are no different than those produced by the Monte Carlo simulation, suggesting that ϕ are produced in accordance to the JETSET predictions. An apparent hardness in the "true" distribution for ζ in gluon jets turned out to be due to inaccuracy in the simulation which was used to model the background.

5.3 $K^{*0} \rightarrow K^+\pi^-$ Analysis

The analysis of the K^{*0} proceeds in much the same way as the ϕ analysis, the principal difference being that one of the decay particles is a pion, hence the combinatorial background under the signal is much higher. Note that no distinction is made here between the decay $K^{*0} \rightarrow K^+\pi^-$ and $\overline{K^{*0}} \rightarrow K^-\pi^+$.

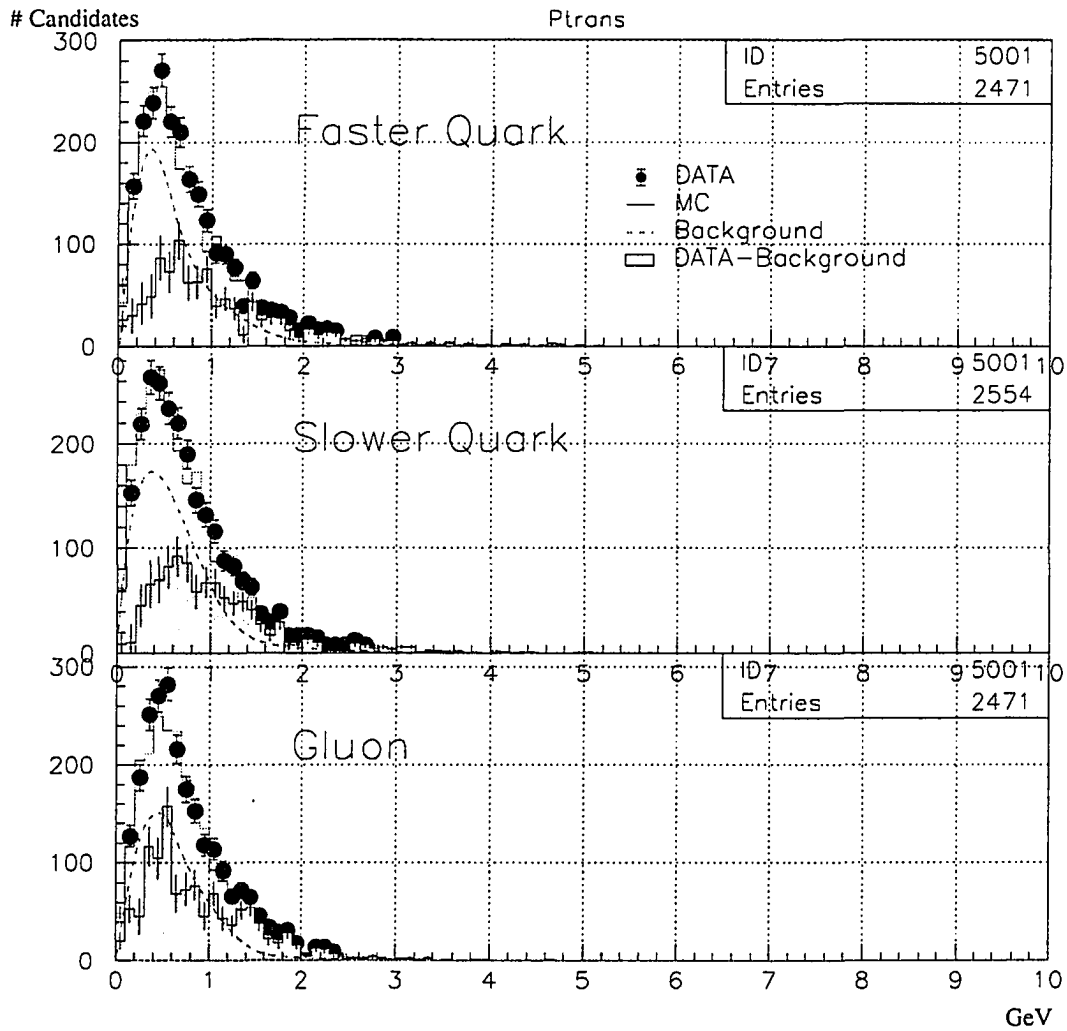

Figure 5.5 ϕ transverse momentum. Note that P_T is not normalized to the jet momentum.

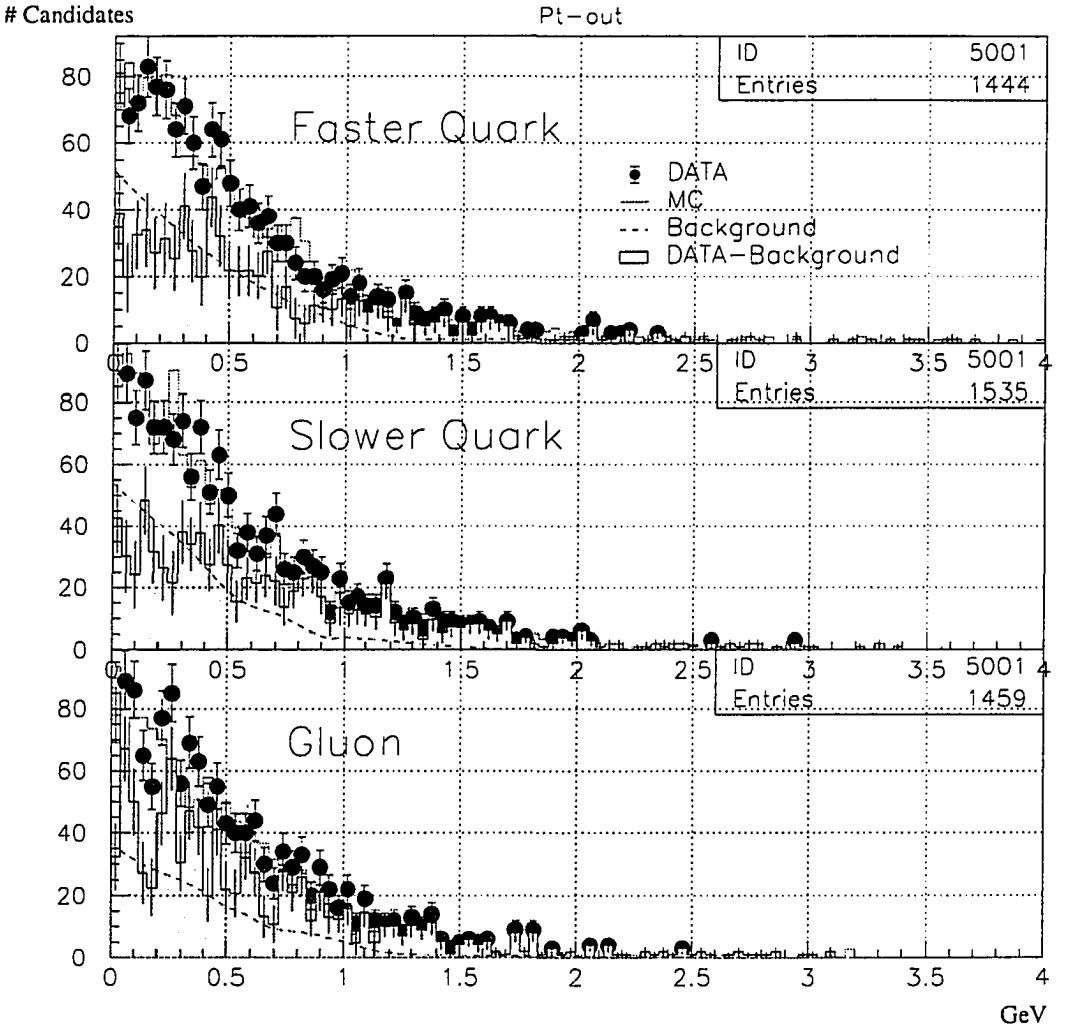

Figure 5.6 ϕ transverse momentum out of the event plane.

As before, kaons are identified using combined information from the liquid RICH, gas RICH, and the TPC. These kaons are paired up with pions (strictly speaking, untagged charged particles) to form K^{*0} candidates (see Figure 5.7). Of these, only those with a combined mass within 50MeV of the K^{*0} mass were used.

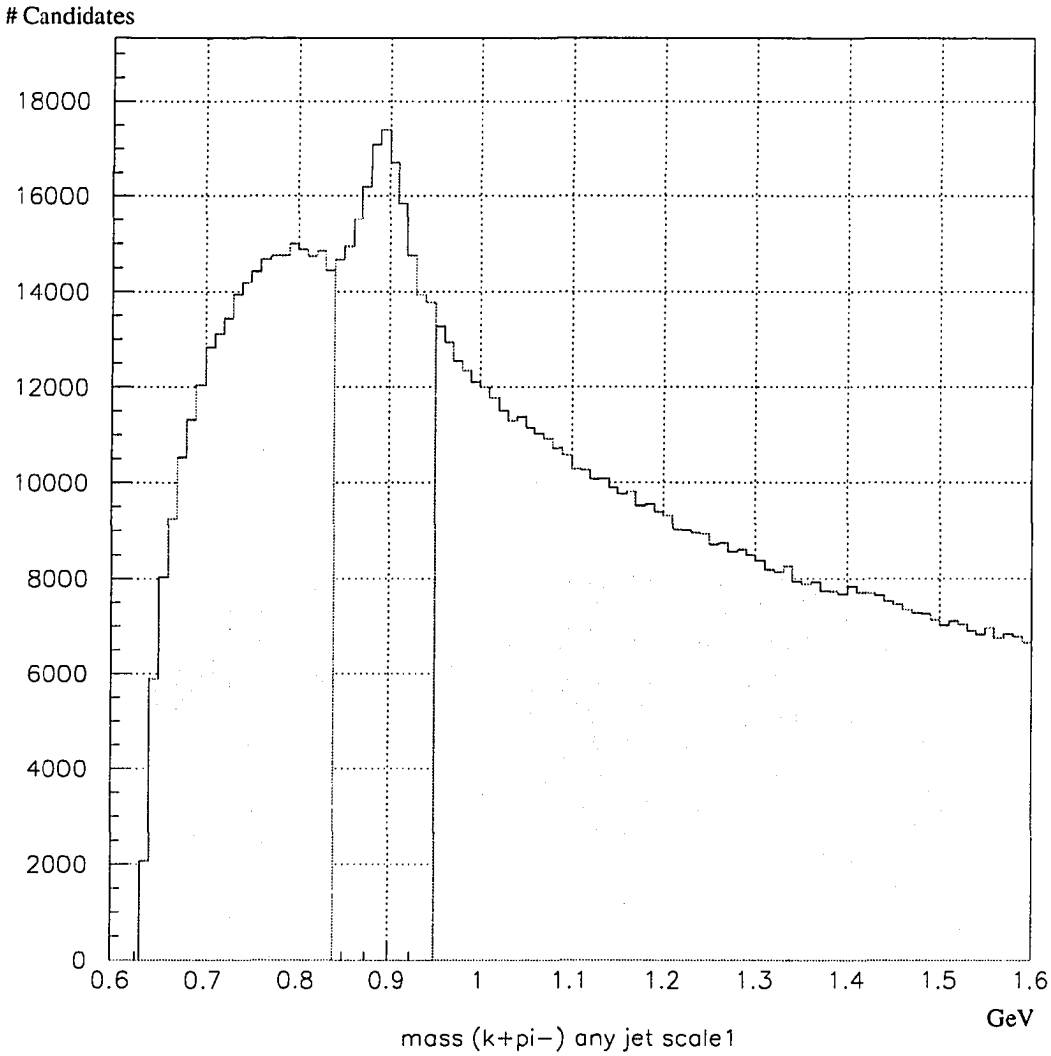

Figure 5.7 $K^{+}\pi^{-}$ invariant mass spectrum showing the K^{*0} peak. The unshaded area represents K^{*0} candidates.

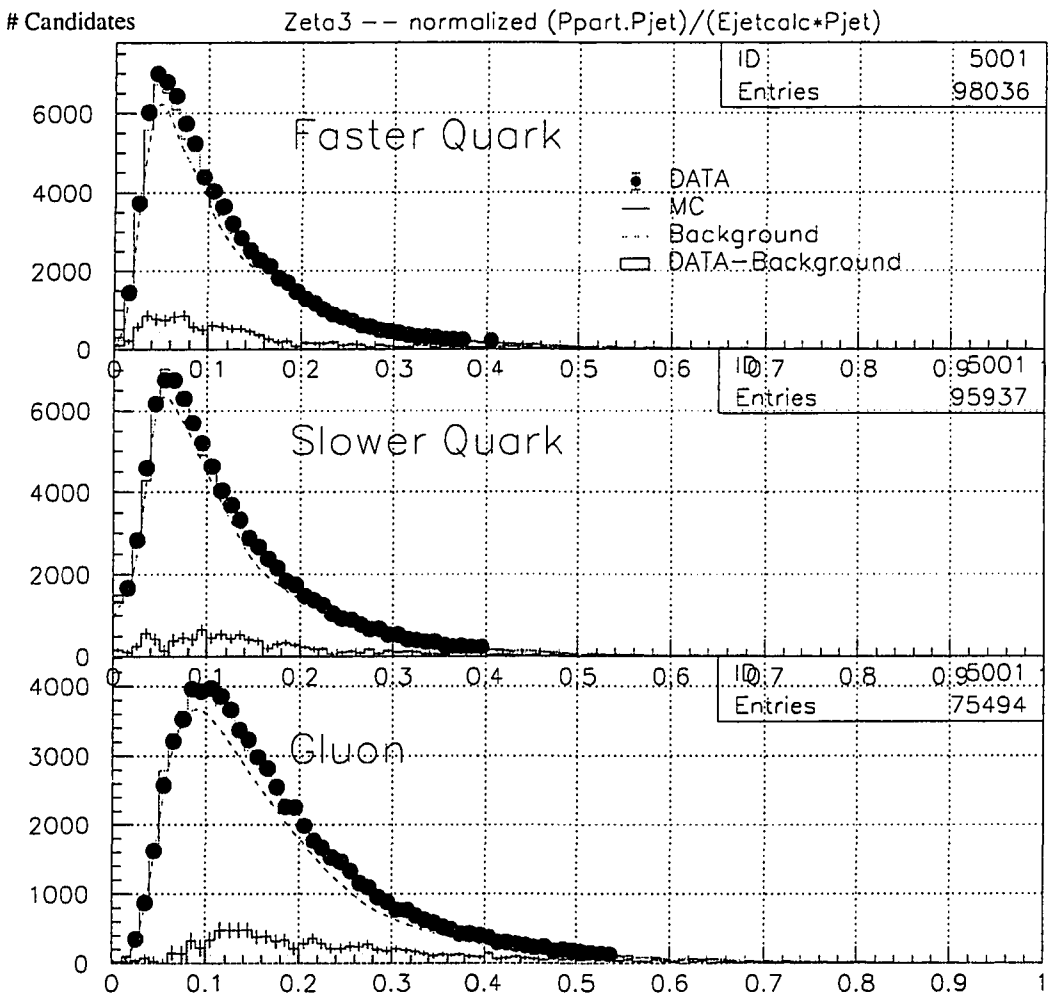

Figure 5.8 ζ, the K^{*0} longitudinal momentum normalized to jet momentum.

5.3.1 Scaled Longitudinal Momentum ζ

As with the ϕ we can plot the longitudinal momentum of the K^{*0} candidate scaled to the jet energy, $\zeta \equiv p_{||}/E_{jet}^{calc}$ (Figure 5.8) to see how much the K^{*0} is a leading particle.

Unlike the ϕ, the fractional longitudinal momentum carried by K^{*0} produced in gluon jets seems to be similar to those produced in quark jets. Admittedly, the large background of false $K^{\pm}\pi^{\mp}$ makes drawing conclusions difficult. There is heavy dependence on the monte carlo to determine the effect of these false combinations.

Plotting the longitudinal momentum without first normalizing to the jet energy (Figure 5.9) yields a plot which is qualitatively similar (to Figure 5.8).

5.3.2 Transverse Momentum P_t

The transverse momentum of K^{*0} compared between quark and gluon jets (Figure 5.10) is essentially the same.

5.3.3 Transverse Momentum Out of the Event Plane P_{T-out}

The transverse momentum out of the event plane, P_{T-out}, looks no different between quark jets and gluon jets (Figure 5.11).

5.3.4 K^{*0} Analysis Summary

No differences were found for K^{*0} production between quark and gluon jets.

5.4 Y-Events

Ideally, one would like to compare quark and gluon jets at the same energy. This removes some of the phase space and boost effects that arise when comparing jets of different energies, allowing a direct comparison to be done. This can be achieved by using Y-events, i.e. events in which there is one fast jet opposite two other jets whose

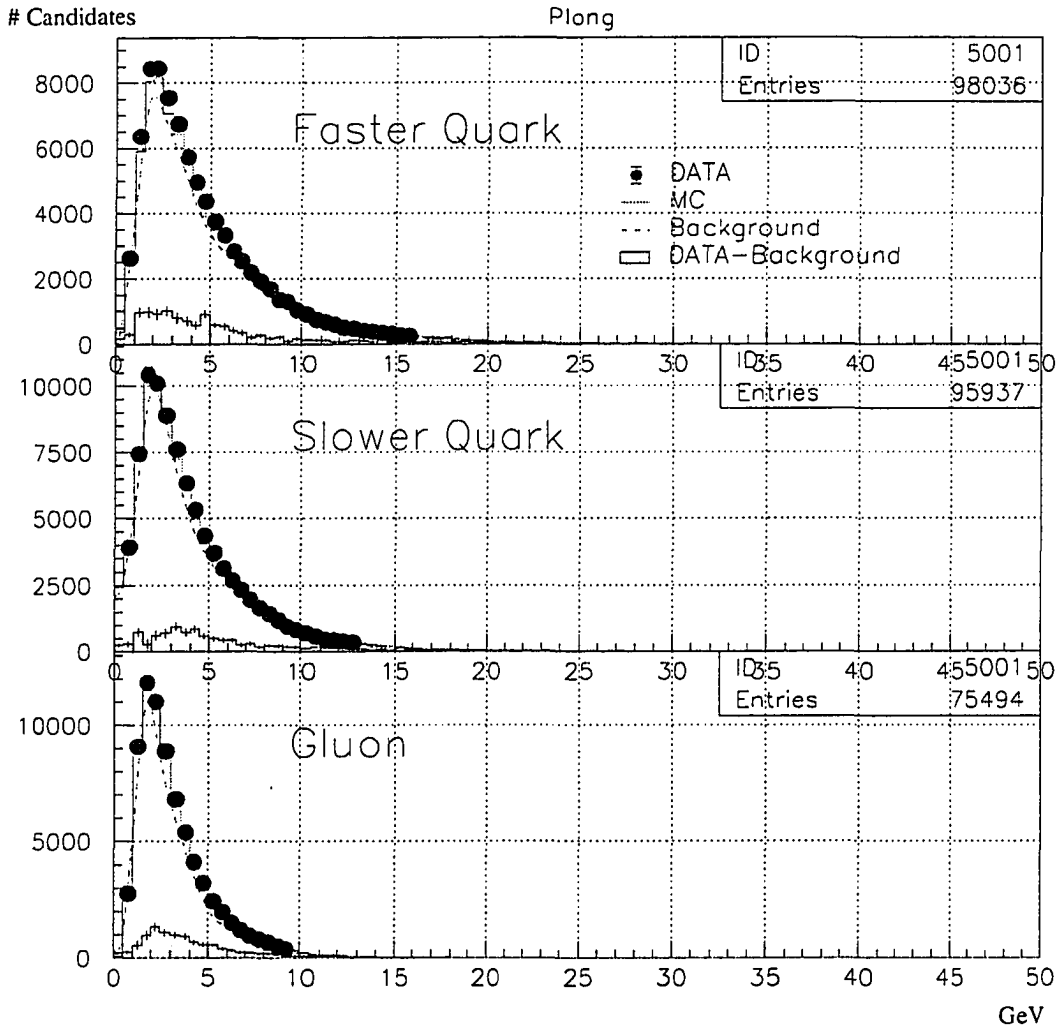

Figure 5.9 K^{*0} longitudinal momentum (unnormalized).

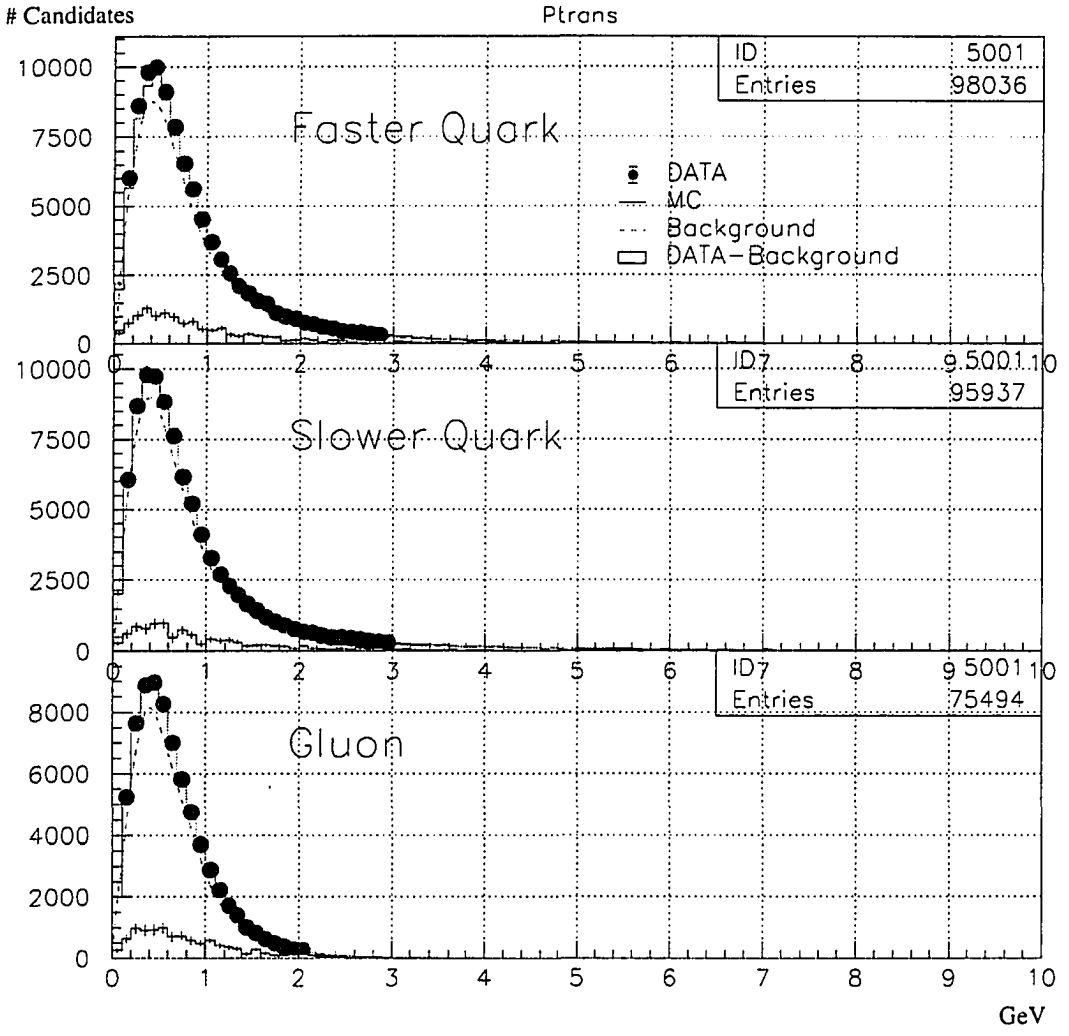

Figure 5.10 K^{*0} transverse momentum.

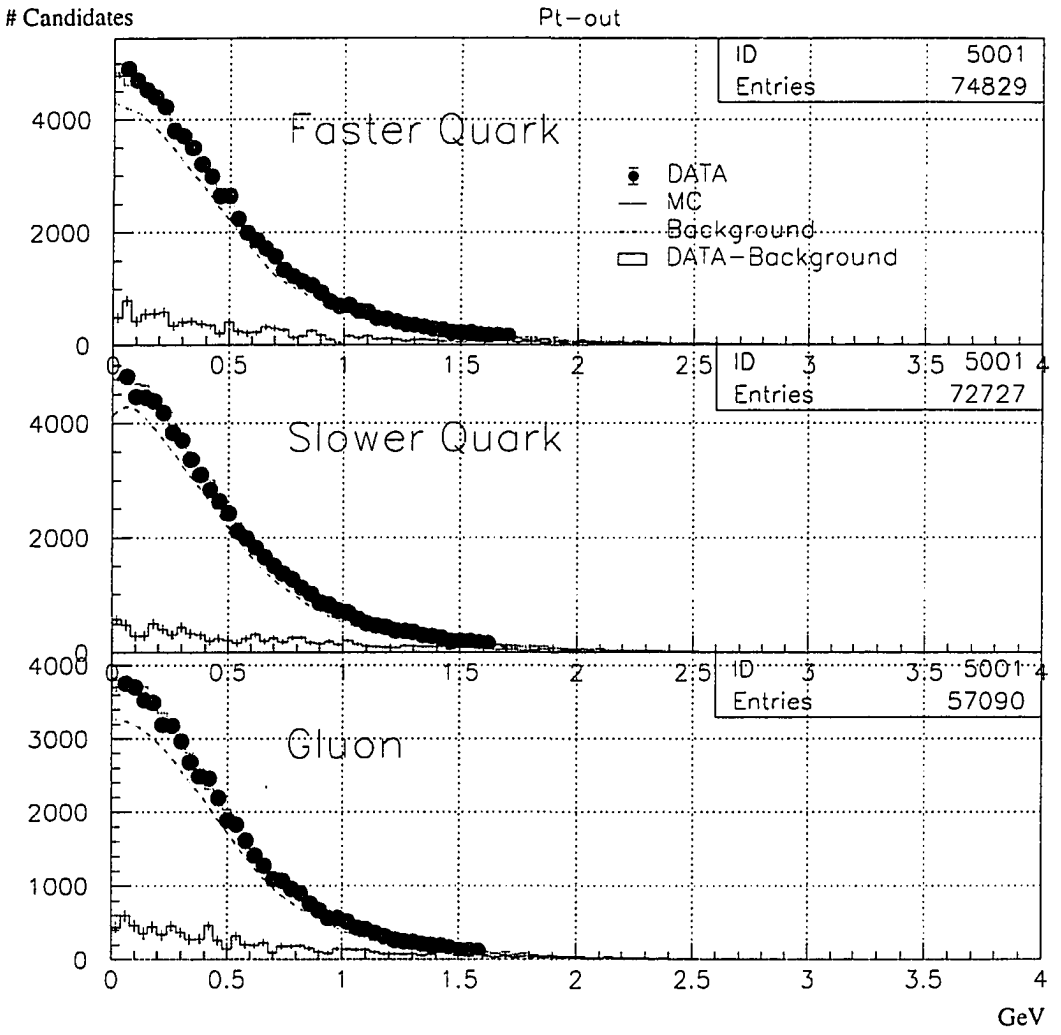

Figure 5.11 K^{*0} transverse momentum out of the event plane.

momenta are equal. In this case, the two "arms" of the Y are likely to be the gluon jet and the jet from the quark which radiated the gluon.

In order to do this comparison, one needs a way to tag the gluon jet. Energy will not work as a tagging variable, as was done in the previous sections, because the jet energies are the same. I investigated using other variables which are different for quark and gluon jets, such as jet broadness and jet multiplicity, but none of them tagged the gluon jets effectively. I tried combining them into a workable selection function by using an artificial neural network algoritm. Unfortunately, getting training data from the analysis to the net and then updating the code for the net was laborious and time consuming due to technical problems with the computing infrastructure tools at CERN and in America. The neural net solution seemed to hold some promise at times but not enough to justify the considerable time and effort necessary to implement it, especially when there was little guarantee it would work. However, this project should be continued.

Recently a technique has been proposed [20] to use transverse momentum to determine the color connectedness of the jets. It calculates a color connection coefficient for each pair of jets and, in a three-jet event, calls the most connected jet the gluon jet. This technique looked promising in the papers but didn't work for this analysis. A future attempt, with more stringent cuts than quoted there, should be tried.

The procedure, had I been able to tag the gluon jet in Y-events, would have been to determine the number of, eg., ϕ's, in quark and gluon jets and then measure the ratio of the number of ϕ's produced in gluon jets to the number in quark jets. Additionally, one would want to take the ratio of the number of ϕ's normalized to the number of charged particles in the jet and compare that ratio between quark and qluon jets since the multiplicity for quark and gluon jets is known to be different. I was able to achieve a tagging purity using the color connection method of only 57%, which was not good enough to do a ratio calculation. Therefore, the comparison of Y-events could not be done in this analysis because there was no reliable method for tagging the gluon jet.

CHAPTER 6 CONCLUSIONS

The ζ distribution for ϕ produced in gluon jets seems to be harder than in quark jets, but this is due only to a difference between the generated particle spectra in JETSET and the distribution in real data. The Monte Carlo is peaked too sharply at lower momentum. Such effects are common since often it is the overal production rate which is matched by the simulation while the details are slighly askew. Overall, no significant difference is observed between the simulation and the data for ϕ prodution in quark and gluon jets, indicating that the string model used in the JETSET simulation does a good job of explaining ϕ production in quark and gluon jets at the Z^0 peak.

Likewise for the K^{*0}, no difference was observed between the JETSET prediction and real data; the LUND string model adequately describes K^{*0} production.

Thus, the production characteristics of ϕ and K^{*0} in quark events at LEP seems to be well modeled by the LUND string model as shown by the good match between monte carlo and real data. Any differences which may exist are not evident. The large combinatorial background under the ϕ and especially the K^{*0} peaks shows why most measurements comparing particle production between quark and gluon jets have been restricted to non-decaying particles or those with long life times. However, despite the difficulty, measurment of the ϕ and K^{*0} production at LEP confirms that nothing new or radical is happening in these channels.

While the fact that no new surprises were found may seem somewhat depressing, in fact it represents yet another triumph for the LUND string model and confirms that current theory gives a good discription of particle production in quark and gluon jets.

REFERENCES

[1] K. Whitten, K. Gailey, and R. Davis, *General Chemistry with Qualitative Analysis*, 3rd ed., (W.B. Saunders Publishing, New York, 1981).

[2] Fermilab web site, *A Brief Overview of High-Energy Physics*, http://www.fnal.gov/pub/hep_overview.html, accessed January 12th, 1999.

[3] B. Bederson, editor, *Phys. Rev.* **D50** (1994) 1173.

[4] Donald Perkins, *Introduction to High Energy Physics*, 3rd ed., (Addison Wesley Publishing, Reading, Massachusetts, 1987).

[5] T. Sjöstrand, Comp. Phys. Comm. **82** (1994) 74.

[6] Knowles, I.G., and Lafferty, G.D, *Hadronization in Z^0 decay*, CERN-PPE/97-040, 02 May 1997.

[7] Ya.I. Azimov, *Phys. Lett.* **B165** (1985) 147.

[8] X. Artru, *Nucl. Phys.* **B70** (1974) 93.

[9] M.G. Bowler, *Zeit. Phys.* **C11** (1981) 169.

[10] B. Andersson, *Zeit. Phys.* **C20** (1983) 317.

[11] B. Andersson, *Phys. Rep.* **97** (1983) 33.

[12] B.R. Webber, *Hadronization*, HEP-PH/9411384.

[13] V. Khoze, *Perturbative universality in QCD jet physics*, HEP-PH/9712396.

[14] S. Lupia and W. Ochs, *Hadron multiplicity as the limit of jet multiplicity at high resolution*, HEP-PH/9709246.

[15] S. Lupia and W. Ochs, *Perturbative QCD description of mean jet and particle multiplicities in e^+e^- annihilation*, HEP-PH/9711255.

[16] W. Ochs, *QCD connections between hadron and jet multiplicities*, HEP-PH/9712295.

[17] W. Ochs, *Recent tests of parton hadron duality in multiparticle final states*, HEP-PH/9709248.

[18] T. Sjöstrand, *Comp. Phys. Comm.* **39** (1985) 347-407.

[19] G. Marchesini and B.R. Webber, *Nucl. Phys.* **B310** (1988); G. Marchesini, *Computer Phys. Comm.* **67** (1992) 465.

[20] R. Orava, *From jets to color portraits of hard scattering final states*, Helsinki Institute of Physics preprint HIP-1997-66/EXP(1997).

[21] P. Abreu et al., *Identified Particles in Quark and Gluon Jets*, DELPHI 96-71 CONF 5, 25 June 1996.

[22] P. Abreu et al., *DELPHI event generation and detector simulation*, DELPHI 89-67 PROG 142.

[23] P. Abreu et al., *Production Characteristics of K^0 and Light Meson Resonances in Hadronic Decays of the Z^0*, CERN-PPE/94-130; Zeit. Phys. **C65** (1995) 587.

[24] P. Abreu et al., *Production of Σ^0 and Ω^- in Z Decays*, CERN-PPE/96-12; Zeit. Phys. **C72** (1996) 17.

[25] P. Abreu et al., *First Measurement of $f_2'(1525)$ Production in Z^0 Hadronic Decays*, CERN-PPE/96-26; *Phys. Lett.* **B379** (1996) 309.

[26] P. Abreu et al., *Measurement of Inclusive π^0 Production in Hadronic Z^0 Decays*, CERN-PPE/95-144; *Zeit. Phys.* **C69** (1996) 561.

[27] P. Abreu et al., *Strange Baryon Production in Z Hadronic Decays*, CERN-PPE/95-39; *Zeit. Phys.* **C67** (1995) 543.

[28] OPAL Collaboration, *Production of K_s^0 and lambda in Quark and Gluon Jets from Z0 Decay*, CERN-EP/98-058.

[29] OPAL Collaboration, *Production of $f_0(980)$, $f_2 1270)$ and phi(1020) in Hadronic Z0 Decay*, CERN-EP/98-010; *Euro. Phys. Journal* **C4** (1998) 19-28.

[30] OPAL Collaboration, *Sigma+, Sigma0 and Sigma- Hyperon Production in Hadronic Z0 Decays*, CERN-PPE/96-100; *Zeit. fur Physik* **C73** (1997) 587-599.

[31] OPAL Collaboration, *Strange Baryon Production in Hadronic Z0 Decays*, CERN-PPE/96-099; *Zeit. fur Physik* **C73** (1997) 569-585.

[32] OPAL Collaboration, *A Model Independent Measurement of Quark and Gluon Jet Properties and Differences*, CERN-PPE/95-075; *Zeit. fur Physik* **C68** (1995) 179-202.

[33] OPAL Collaboration, *Inclusive Strange Vector and Tensor Meson Production in Hadronic Z Decays*, CERN-PPE/95-027; *Zeit. fur Physik* **C68** (1995) 1-11.

[34] ALEPH Collaboration, *Inclusive Production of Neutral Pions in Hadronic Z Decays*, CERN-PPE/96-168; *Zeit. fur Physik* **C74** (1997) 451.

[35] J. Donoghue, E. Golowich, and B. Holstein, *Dynamics of the Standard Model*, (Cambridge University Press, Cambridge, 1992).

[36] B. Bederson, editor, *Phys. Rev.* **D50** (1994) 1247.

[37] D. Lane and R. McKay, *Informal measurement of the amperage of two common flashlights in the electronics lab down the hall*, January 14th, 1999. [Unpublished results.]

[38] DELPHI Collaboration, *Performance of the DELPHI Detector*, CERN-PPE/95-194, 21 December 1995.

[39] DELPHI Collaboration, *DELSIM User Manual*, DELPHI 87-96 PROG 99, 1989; DELSIM Reference Manual, DELPHI 87-98 PROG 100, 1989.

[40] DELPHI Collaboration, *DELANA User's Guide*, DELPHI 89-44 PROG 137, 1989.

[41] S. Catani et al., *Phys. Lett.* **B269** (1991) 432.

[42] JADE Collaboration, *Phys. Lett.* **C33** (1986) 23; S. Bethke et al., *Phys. Lett.* **B213** (1988) 235.

ACKNOWLEDGEMENTS

I would like to thank Jerry Lamsa for his help in choosing a viable thesis topic, Bert Crawley, Tom Meyer, and Alex Firestone for enlightening discussions on experimental particle physics, and my advisor Eli Rosenberg for his guidance of my thesis work. Special thanks and a grateful note of appreciation is due to Linda Shuck for all the help and support she gave me throughout my graduate career, both administratively and as a friend. I thank my parents Roy and Nora Lane for raising me to have an inquiring mind and to love learning, my brother Bryan Lane who has always supported me both as my brother and as my best friend, and my sisters Audrey Cortez and Heather Clark for their role in the early education of their little brother. In addition, Alan Donley, Lance Caughfield, and Dia Sharbono deserve recognition for keeping in touch and boosting my morale throughout my graduate career. Finally, I thank Kim Brittingham for helping me make it through the final months during which I was writing my thesis. Without all these people, I would have given up hope long ago and sought release in a more mundane livelihood far removed from experimental high energy physics.

This work was supported in part by the U.S. Department of Energy under grant number DE-FG02-94ER40817.

IMAGE EVALUATION TEST TARGET (QA-3)

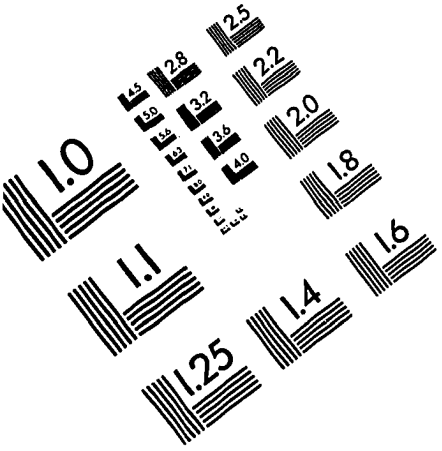

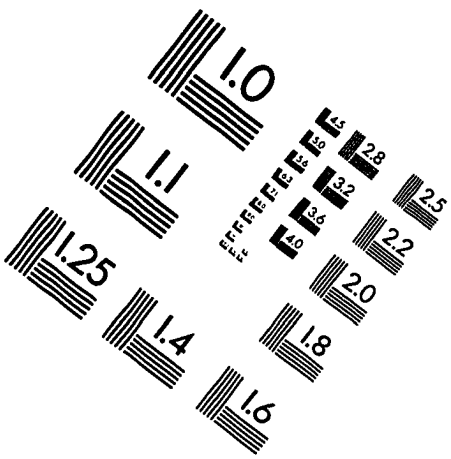

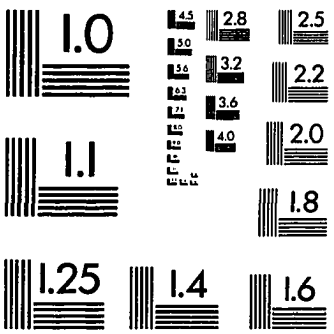

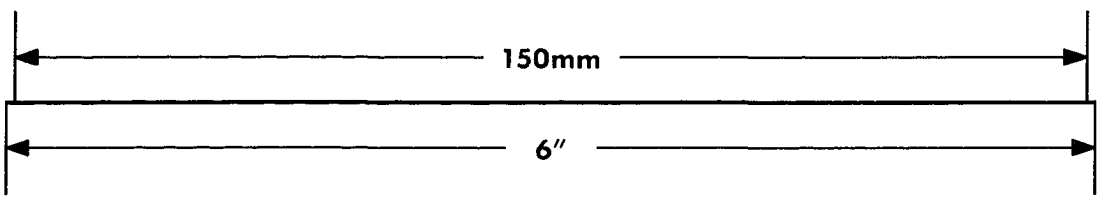

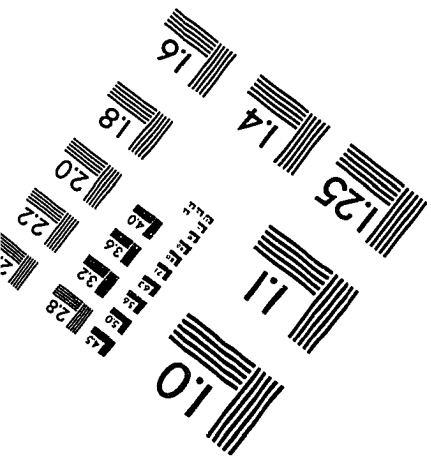

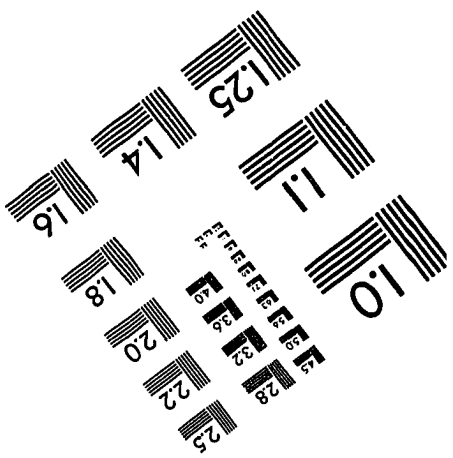

APPLIED IMAGE, Inc
1653 East Main Street
Rochester, NY 14609 USA
Phone: 716/482-0300
Fax: 716/288-5989